

Article

Observation of the axion quasiparticle in 2D MnBi₂Te₄

<https://doi.org/10.1038/s41586-025-08862-x>

Received: 14 August 2024

Accepted: 4 March 2025

Published online: 16 April 2025

 Check for updates

Jian-Xiang Qiu¹, Barun Ghosh^{2,3,4}, Jan Schütte-Engel^{5,6}, Tiema Qian⁷, Michael Smith⁸, Yueh-Ting Yao⁹, Junyeong Ahn¹⁰, Yu-Fei Liu^{1,10}, Anyuan Gao¹, Christian Tzschaschel^{1,11}, Houchen Li¹, Ioannis Petrides¹², Damien Bérubé¹, Thao Dinh^{1,10}, Tianye Huang¹, Olivia Liebman^{12,13}, Emily M. Been¹², Joanna M. Blawat¹⁴, Kenji Watanabe¹⁵, Takashi Taniguchi¹⁵, Kin Chung Fong^{2,3,16}, Hsin Lin¹⁷, Peter P. Orth^{18,19,20}, Prineha Narang^{12,21}, Claudia Felser²², Tay-Rong Chang^{9,23,24}, Ross McDonald¹⁴, Robert J. McQueeney^{18,19}, Arun Bansil^{1,2,3}, Ivar Martin⁸, Ni Ni⁷, Qiong Ma^{25,26}, David J. E. Marsh²⁷, Ashvin Vishwanath¹⁰ & Su-Yang Xu^{1,2*}

The axion is a hypothetical fundamental particle that is conjectured to correspond to the coherent oscillation of the θ field in quantum chromodynamics^{1,2}. Its existence would solve multiple fundamental questions, including the strong CP problem of quantum chromodynamics and dark matter, but the axion has never been detected. Electrodynamics of condensed-matter systems can also give rise to a similar θ , so far studied as a static, quantized value to characterize the topology of materials^{3–5}. Coherent oscillation of θ in condensed matter has been proposed to lead to physics directly analogous to the high-energy axion particle—the dynamical axion quasiparticle (DAQ)^{6–23}. Here we report the observation of the DAQ in MnBi₂Te₄. By combining a two-dimensional electronic device with ultrafast pump–probe optics, we observe a coherent oscillation of θ at about 44 gigahertz, which is uniquely induced by its out-of-phase antiferromagnetic magnon. This represents direct evidence for the presence of the DAQ, which in two-dimensional MnBi₂Te₄ is found to arise from the magnon-induced coherent modulation of the Berry curvature. The DAQ also has implications in light–matter interaction and coherent antiferromagnetic spintronics²⁴, as it might lead to axion polaritons and electric control of ultrafast spin polarization^{6,15–20}. Finally, the DAQ could be used to detect axion particles^{21–23}. We estimate the detection frequency range and sensitivity in the millielectronvolt regime, which has so far been poorly explored.

In optically driven quantum materials, phonons—coherent modulation of the lattice—can markedly modify the electronic structure, leading to exotic non-equilibrium phenomena^{25–27} such as light-induced superconductivity²⁶ and phonon switch of Weyl fermions²⁷. Beyond phonons, quantum materials have many other collective excitations, suggesting handles to engineer electronic structure at ultrafast timescales. Magnets have coherent oscillation of spins—magnons^{28–30}. Specifically, in two-dimensional (2D) MnBi₂Te₄, the antiferromagnetic Mn spins couple with the low-energy surface Dirac bands, giving rise to large Berry curvatures. A fundamentally interesting question is how the Berry curvature will be modulated by the magnons. Interestingly, the

magnon-induced ultrafast Berry curvature modulation in 2D MnBi₂Te₄ also leads to a dynamical axion quasiparticle (DAQ) that is directly analogous to the high-energy axion particle.

In particle physics, the axion is a boson generated by the coherent oscillation of the θ field^{1,2} (where θ is the CP violating term in quantum chromodynamics; see Fig. 1a). This particle is of importance in quantum chromodynamics, cosmology and string theory^{1,2}. However, owing to the weak interaction with normal matter, the search for axion has been a challenging problem. In condensed matter, a similar θ was introduced³ as a static value, which is proportional to a material's magnetoelectric coupling $\theta = \pi \frac{2h}{e^2} \alpha$ (h , Planck constant; e , elementary charge;

¹Department of Chemistry and Chemical Biology, Harvard University, Cambridge, MA, USA. ²Department of Physics, Northeastern University, Boston, MA, USA. ³Quantum Materials and Sensing Institute, Northeastern University, Burlington, MA, USA. ⁴Department of Condensed Matter and Materials Physics, S. N. Bose National Centre for Basic Sciences, Kolkata, India. ⁵Department of Physics, University of California, Berkeley, Berkeley, CA, USA. ⁶RIKEN iTHEMS, Wako, Saitama, Japan. ⁷Department of Physics and Astronomy and California NanoSystems Institute, University of California, Los Angeles, Los Angeles, CA, USA. ⁸Materials Science Division, Argonne National Laboratory, Lemont, IL, USA. ⁹Department of Physics, National Cheng Kung University, Tainan, Taiwan. ¹⁰Department of Physics, Harvard University, Cambridge, MA, USA. ¹¹Department of Physics, University of Zurich, Zurich, Switzerland. ¹²College of Letters and Science, University of California, Los Angeles, Los Angeles, CA, USA. ¹³Department of Materials Science and Engineering, University of California, Los Angeles, Los Angeles, CA, USA. ¹⁴National High Magnetic Field Laboratory, Los Alamos National Laboratory, Los Alamos, NM, USA. ¹⁵National Institute for Materials Science, Tsukuba, Japan. ¹⁶Department of Electrical and Computer Engineering, Northeastern University, Boston, MA, USA. ¹⁷Institute of Physics, Academia Sinica, Taipei, Taiwan. ¹⁸Department of Physics and Astronomy, Iowa State University, Ames, IA, USA. ¹⁹Ames National Laboratory, Ames, IA, USA. ²⁰Department of Physics, Saarland University, Saarbrücken, Germany. ²¹Electrical and Computer Engineering Department, University of California, Los Angeles, Los Angeles, CA, USA. ²²Max Planck Institute for Chemical Physics of Solids, Dresden, Germany. ²³Center for Quantum Frontiers of Research and Technology (QFort), Tainan, Taiwan. ²⁴Physics Division, National Center for Theoretical Sciences, Taipei, Taiwan. ²⁵Department of Physics, Boston College, Chestnut Hill, MA, USA. ²⁶The Schiller Institute for Integrated Science and Society, Boston College, Chestnut Hill, MA, USA. ²⁷Theoretical Particle Physics and Cosmology, King's College London, London, UK. ^{*}e-mail: suyangxu@fas.harvard.edu

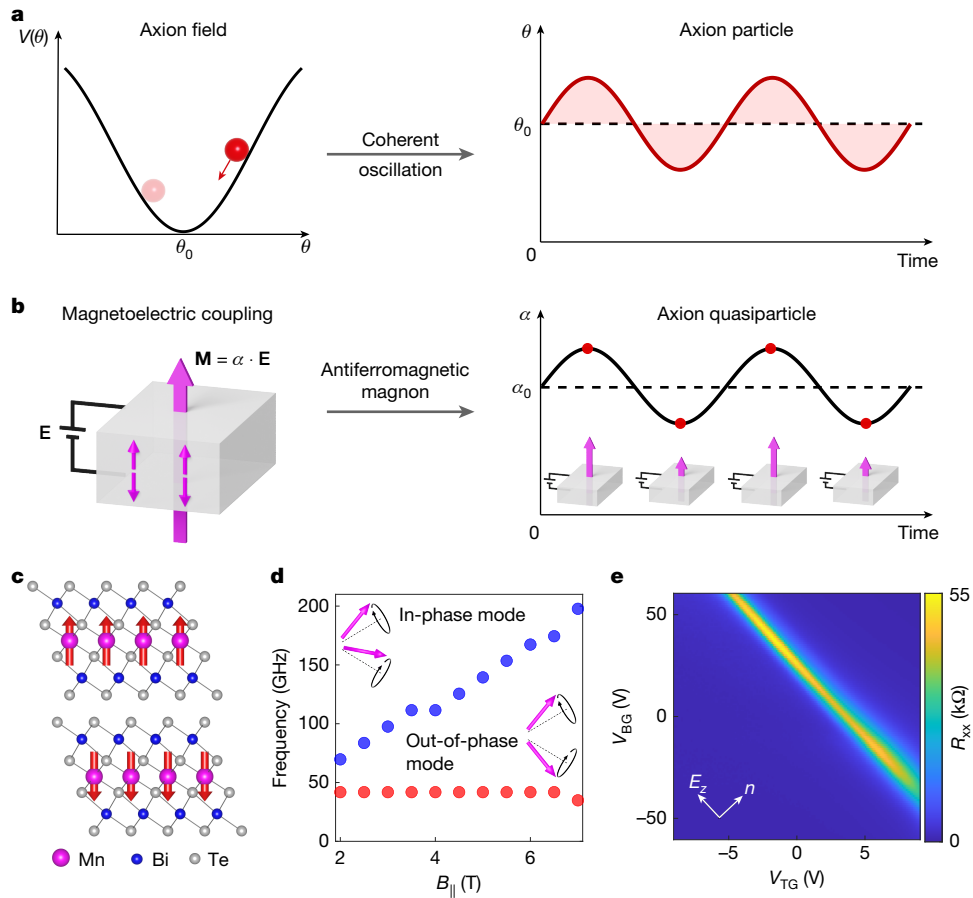


Fig. 1 | Axion particle and quasiparticle and basic information of 2D MnBi₂Te₄.

a, The axion particle is the coherent oscillation of the θ field in quantum chromodynamics^{1,2} ($V(\theta)$ is the axion potential for the θ field; θ_0 is the static θ angle). **b**, In condensed matter, the θ angle is directly proportional to the trace of the magnetoelectric coupling, $\theta = \pi \frac{2\eta}{3e^2} \sum_{i=x,y,z} \alpha_{ii}$ (the purple arrows represent the electric field induced magnetization). The DAQ is the coherent oscillation of the magnetoelectric coupling (α_0 is the static magnetoelectric coefficient). **c**, MnBi₂Te₄ has a centrosymmetric rhombohedral lattice structure (the non-magnetic group is $-3m$). It has a layered antiferromagnetic order (the red arrows represent the magnetic spins), where Mn spins within a layer are

ferromagnetic with an out-of-plane easy axis and Mn spins between two adjacent layers are antiparallel (the magnetic group of an even-layer 2D MnBi₂Te₄ is $-3'm'$). **d**, Experimentally measured frequencies for the in-phase magnon and out-of-phase magnon modes as a function of the in-plane magnetic field B_{\parallel} of six-layer MnBi₂Te₄ (the insets illustrate the spin precession of the two magnon modes). See schematics in Extended Data Fig. 1a–d for a detailed visualization of the magnon modes. **e**, The dual-gate resistance map for a six-layer MnBi₂Te₄ electrical device (V_{BG} , back gate voltage; V_{TG} , top gate voltage; R_{xx} , longitudinal resistance).

α , magnetoelectric coefficient). In the presence of time-reversal T or space-inversion P symmetry, θ is quantized in insulators and it describes the topological invariant. Experimental studies of the static θ have led to breakthroughs, generating great interest^{4,5,31}. Beyond the static θ , the coherent oscillation of θ is proposed to lead to new physics directly analogous to the high-energy axion particle, the DAQ. When T and P symmetries are both broken (for example, in certain antiferromagnetic insulators), θ can coherently oscillate when coupled to certain magnetic fluctuations, giving rise to the DAQ. Since the initial prediction by ref. 6, the DAQ has attracted great interest and has been anticipated by many theoretical works^{6–23}. The key motivations driving these theoretical interests are as follows. (1) The DAQ enables a wide range of quantum electromagnetic and spin phenomena^{6,15–20}. (2) The DAQ provides a condensed-matter simulation of the high-energy axion particle. (3) Beyond a simulator, the DAQ can be used as a detector of the axion particle^{21–23}.

In principle, any antiferromagnetic material that breaks T and P can host the DAQ. However, in most systems, both topologically non-trivial and trivial, the DAQ turns out to be very weak⁸: that is, the coherent oscillation of θ is very weak even under a strong magnetic fluctuation. Also, the DAQ needs to be driven by specific magnetic fluctuations.

Previous theoretical works considered the antiferromagnetic amplitude mode^{6,8–10}, which is difficult to excite experimentally. These challenges have hindered the experimental detection of the DAQ. On a separate front, beyond antiferromagnetic insulators, the dynamical θ has also been proposed to arise from the phason (sliding mode) of the charge-density-wave state in Weyl semimetals. Promising d.c. transport evidence has been reported in Ta₂Se₈I (ref. 32), but definitive demonstration remains lacking³³. In this paper, we make critical conceptual advances to bridge theory and experiments including: (1) identifying an antiferromagnetic system that features a large DAQ; (2) figuring out a magnetic fluctuation that can induce the DAQ but is much more experimentally accessible; and (3) developing an experimental scheme that can directly measure the θ oscillation. Previous studies have investigated the optical detection as well as the ultrafast magnon dynamics in MnBi₂Te₄, CrI₃ and Cr₂Ge₃Te₆ (refs. 34–40). In particular, ref. 36 systematically studied the dynamics of the out-of-phase magnons in MnBi₂Te₄ and ref. 40 reported the antiferromagnetic Kerr effect in even-layer MnBi₂Te₄. These studies provide important knowledge that guides our work here. As such, we present the observation of the DAQ, driven by the out-of-phase antiferromagnetic magnons under an in-plane magnetic field in 2D even-layer MnBi₂Te₄.

Basic characterization

Figure 1c shows a side view of 2D even-layer MnBi_2Te_4 (refs. 34–39, 41–52). The crystal structure is centrosymmetric, but the layered antiferromagnetic order breaks both time-reversal and space-inversion symmetries (the Mn spins have an out-of-plane easy axis). As such, 2D even-layer MnBi_2Te_4 is a possible platform to host the DAQ, as predicted by both symmetry analysis and theoretical calculations in ref. 10.

We study the antiferromagnetic magnons in 2D even-layer MnBi_2Te_4 , focusing on the scenario in the presence of an in-plane static magnetic field B_{\parallel} as it is most relevant to our experiments. The B_{\parallel} cant the Mn spins away from the out-of-plane easy axis, where the equilibrium spin directions under finite B_{\parallel} are indicated by the dashed lines in Fig. 1d. Supplementary Information section I.6 shows additional measurements to validate such evolution. The magnons are spin precessions away from the dashed lines. Considering the two antiferromagnetic sublattices, there are naturally two magnon modes, where the spin precessions of the antiferromagnetic sublattices have the same phase (the in-phase mode) or opposite phase (the out-of-phase mode). Extended Data Fig. 1a,b shows the complete time evolution of the spin precessions. Moreover, it is informative to study the projection of the spins to the \hat{z} axis (S_z). As shown in Extended Data Fig. 1c,d, for the out-of-phase mode, the net out-of-plane magnetization $M_z = S_{1z} + S_{2z}$ is zero. For the in-phase mode, by contrast, the net magnetization M_z is non-zero and it oscillates as a function of time. We have characterized their resonant frequencies as a function of B_{\parallel} (ref. 53; Methods). As shown in Fig. 1d, the in-phase magnon frequency increases monotonically with B_{\parallel} ; the out-of-phase magnon frequency remains roughly invariant and starts to slightly decrease at 7 T. Strictly speaking, 6SL (where SL denotes septuple layer) has six magnon modes. In Supplementary Information section I.2.1, we present thorough discussion in connection with our experimental data.

Next, we have made dual-gated electrical devices with six-layer MnBi_2Te_4 . The combination of the top and bottom gates allows us to control the charge density n and the out-of-plane electric field E_z independently. We keep the Fermi level inside the gap at $n = 0$ unless otherwise noted. Also, we studied the E -field dependence by the lock-in method where E was a.c. modulated (see ‘How we measured the DAQ’ in Methods). Figure 1e shows its resistance gate map, where the charge neutrality resistance peak is observed.

Static θ measurements

The DAQ is a coherent oscillation of $\theta(t)$ (t denotes time), which directly manifests as a coherent oscillation of the magnetoelectric coupling $\alpha(t)$ because of their proportionality ($\theta = \frac{\pi}{e^2} \frac{2h}{\epsilon^2} \alpha$). Before searching for the time-dependent oscillation, we first study the static magnetoelectric coupling α . The magnetoelectric coupling is defined as the electric-field-induced magnetization $\alpha = \frac{dM}{dE}$. Experimentally, we measure α by measuring the E -induced Kerr effect while keeping the Fermi level always at charge neutrality $n = 0$ (unless otherwise noted). Specifically, an out-of-plane electric field E_z is applied by the dual gates; we use the optical Kerr rotation under normal incidence to measure the net out-of-plane magnetization, Kerr rotation = M_z/y , where y is a material-specific conversion coefficient (Supplementary Information sections I.3 and II present additional studies including symmetry analysis, wavelength dependence, and simultaneous Kerr and Faraday data that further strengthen the conclusion that our E -field-induced Kerr rotation measures the E -field induced M_z). Therefore, we measure α by measuring the slope of the Kerr rotation with respect to E_z , that is, $\alpha = y \frac{d\text{Kerr rotation}}{dE_z}$.

Indeed, our data in Fig. 2b show that the measured Kerr rotation increases linearly with increasing E_z . Its slope is proportional to the magnetoelectric coupling α . We then studied the temperature dependence of α (Fig. 2c): α is the largest at the base temperature and decreases

to zero at the Neel temperature T_N . We also studied α in the opposite antiferromagnetic state (Fig. 2e,f), which shows the opposite sign. We further studied the spatial dependence. As shown in Fig. 2g, our data reveal homogeneous α across the entire device. As a side point, this also demonstrates a way to spatially resolve antiferromagnetic domains, which has been challenging. Moreover, we have converted α from the unit of $\mu\text{rad V}^{-1} \text{nm}$ (left axis) to the unit of $e^2/2h$ (right axis) (Methods). We also studied the in-plane magnetic field B_{\parallel} dependence (Fig. 2h). We found that α monotonically decreases as B_{\parallel} cant the equilibrium spin directions away from the out-of-plane easy axis.

Observing the dynamical axion quasiparticle

Now that we have individually characterized the magnons and the static θ , we combine them to search for the ultrafast coherent oscillation of θ . To this end, we construct an experimental set-up that combines ultrafast pump-probe optics with 2D electronic devices. As shown in Fig. 3a, the pump laser launches coherent magnons (both the in-phase and the out-of-phase modes). The probe detects the magnetoelectric coefficient α , which is measured by E_z -induced Kerr rotation. By varying the delay time t between the pump and probe, we can measure the time-dependent magnetoelectric coupling with femtosecond resolution $\alpha(t)$. It is noted that the time-dependent magnetoelectric coupling contains a static component and a pump-induced dynamical change, $\alpha(t) = \alpha_{\text{static}} + \Delta\alpha(t)$. The α_{static} has been studied above, so we focus on $\Delta\alpha(t)$.

Figure 3c shows the most essential dataset of our study here: the x axis is the delay time t ; the y axis is the pump-induced dynamical change of the magnetoelectric coupling $\Delta\alpha(t)$; and the in-plane magnetic field B_{\parallel} is 6 T. From the data, we clearly observe a coherent oscillation of magnetoelectric coefficient $\alpha(t)$ ($\sim \theta(t)$), therefore demonstrating the DAQ by its definition.

Interestingly, the magnitude of α oscillation is quite large: the $\Delta\alpha(t)$ oscillation reaches $0.05 e^2/2h$ (right axis of Fig. 3c), which is 12% of the static α at the corresponding magnetic field $B_{\parallel} = 6$ T (Fig. 2h). The fast Fourier transform (inset of Fig. 3c) shows a distinct resonance at about 44 GHz, consistent with the out-of-phase magnon mode. The underlying out-of-phase magnon oscillation (arrows in Fig. 3c) are drawn synchronized with the observed α oscillation, which allows us to directly visualize how the coherent spin precession controls α at different time point. Interestingly, although both the in-phase and out-of-phase magnons are launched by the pump laser, only the out-of-phase magnons directly couple to the θ field in MnBi_2Te_4 , giving rise to a coherent oscillation of θ , which is explained in the next section.

To further substantiate our conclusion, we perform systematic measurements. First, it is important to check that we are really measuring the α oscillation in Fig. 3c. In other words, each data point of $\Delta\alpha$ in Fig. 3c should correspond to the slope between pump-induced Kerr and electric field E_z (see also Extended Data Fig. 2). This is explicitly checked in Fig. 3b, where the pump-induced ΔKerr ($\propto \Delta M_z$) shows a linear dependence on E_z . Therefore, all ΔM_z observed in Fig. 3b are induced by the electric field. Comparing Fig. 3b,c directly, the slope for 1 ps and 9 ps in Fig. 3b is opposite. Correspondingly, the $\Delta\alpha(t)$ at 1 ps and 9 ps in Fig. 3c indeed show opposite sign. Second, we measure $\Delta\alpha(t)$ as a function of the in-plane magnetic field B_{\parallel} , where the raw data are shown in Fig. 3d. By performing fast Fourier transform on every time trace, we found (Fig. 3f) that the resonant frequency shows weak dependence on B_{\parallel} , again confirming that the observed DAQ is induced by the out-of-phase magnons. Third, we performed temperature-dependent measurements. As shown in Fig. 3e,g, we found a critical slowdown behaviour, that is, the resonance frequency decreases to zero at the transition temperature. In addition, it is crucial to check that the magnetic properties such as exchange coupling, anisotropy and magnon frequency of MnBi_2Te_4 are not significantly changed by gates. Supplementary Information sections I.3, I.4 and II

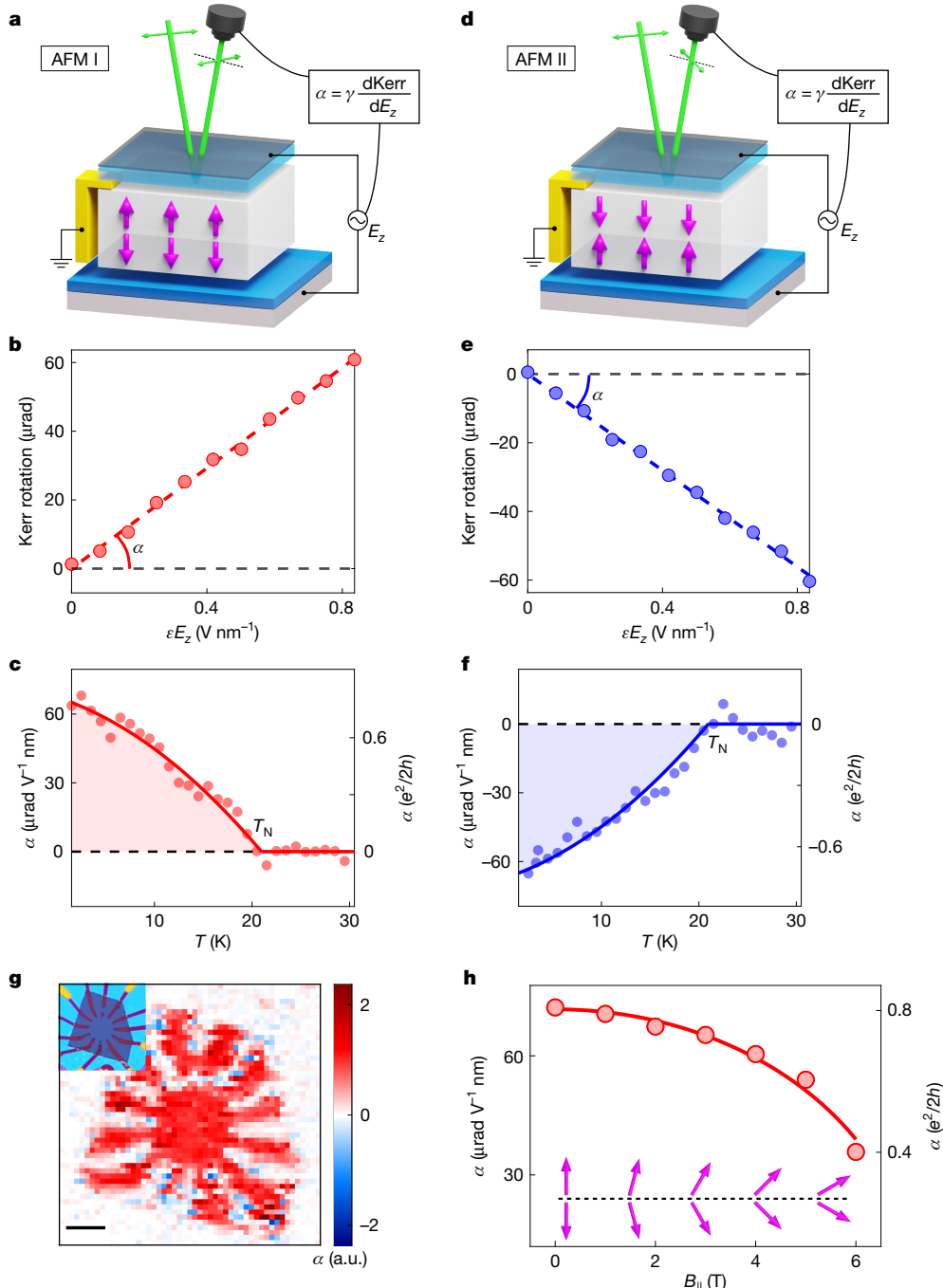


Fig. 2 | Probing the static magnetoelectric coupling in 2D MnBi_2Te_4 . **a**, Schematic experimental set-up to probe the static magnetoelectric coupling. The out-of-plane electric field E_z is applied by the top and bottom gates. The E_z -induced magnetization is measured by the optical Kerr rotation under normal incidence. Hence, α is measured by $\frac{d\text{Kerr}}{dE_z}$. **b**, Measured Kerr rotation as a function of a.c. E_z modulation for our six-layer MnBi_2Te_4 device (ε , permittivity). The slope here is α . **c**, Measured α as a function of temperature. We have converted α from the unit of $\mu\text{rad V}^{-1}\text{nm}$ (left axis) to the unit of $e^2/2h$ (right axis) (Methods). The shaded area highlights the fitting curve. Supplementary Information section II.2 shows the d.c. E_z dependence, which yields consistent

results for α . **d–f**, The same as panels **a–c**, respectively, but for the opposite antiferromagnetic (AFM) domain. **g**, Spatial map of the measured α over the entire device (the inset shows an optical microscopy image of the device). Scale bar, 10 μm . **h**, Measured α as a function of $B_{||}$ (the inset (bottom) shows the evolution of the AFM order with the in-plane magnetic field). The probe wavelength was 515 nm. Supplementary Information section I.3 shows the wavelength-dependent data. The sample was cooled with a parallel $\mathbf{E} \cdot \mathbf{B}$ field. Depending on the sign of $\mathbf{E} \cdot \mathbf{B}$, the sample was prepared into a specific antiferromagnetic state. All measurements were performed at normal incidence. The small incidence angle is only an artistic choice.

present additional systematic magneto-optical Kerr effect (MOKE) measurements, including d.c. gate dependence and similar measurements in odd layer MnBi_2Te_4 , which demonstrate that within the experimental E and n ranges studied here, the magnetic properties are roughly invariant. We also present additional measurements to

assess the sample quality following the processing of the electric contacts and to disentangle magnon and phonon origin for the observed DAQ (Supplementary Information sections I.3 and I.5). These systematic studies further strengthen our experimental observation of the DAQ.

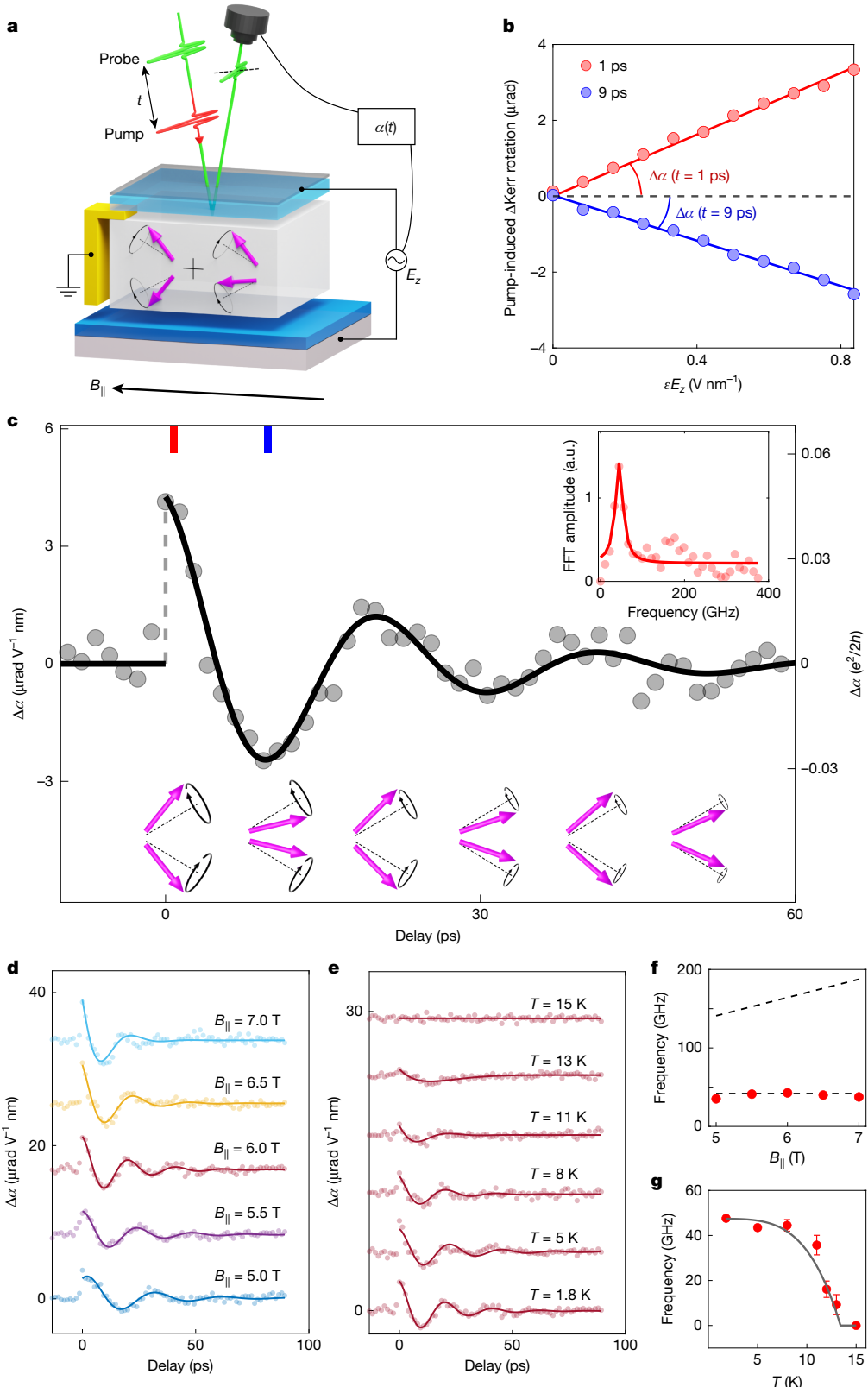


Fig. 3 | Observation of the dynamical axion quasiparticle in 2D MnBi_2Te_4 .

a, Schematic experimental set-up to probe the time-dependent magnetoelectric coupling. The pump laser launches coherent magnons; the probe laser, combined with the dual gate E_z , measures $\frac{d\text{Kerr rotation}}{dE_z}$; by varying the delay time t , we can measure pump-induced $\Delta\alpha(t)$ with femtosecond resolution. **b**, Measured pump-induced Kerr rotation $\Delta\text{Kerr}(t)$ as a function of E_z and t . **c**, Measured pump-induced $\Delta\alpha(t)$ at $B = 6$ T (the red and blue bars correspond to a delay time of 1 ps and 9 ps). A clear oscillation of $\alpha(t)$ provides the experimental observation of

the DAQ. Inset: fast Fourier transform (FFT) of the data. The bottom inset schemes illustrate the spin precession process of the out-of-phase magnon. **d,e**, $\Delta\alpha(t)$ at different $B_{||}$ (**d**) and temperature (**e**) values. The curves are offset for clarity. **f,g**, Fast Fourier transform of the data in **d** and **e**, respectively (the two dashed lines in **f** correspond to in-phase and out-of-phase magnon dispersions). The error bars in **g** represent one standard deviation from the fitting parameters. The small incidence angle is only an artistic choice.

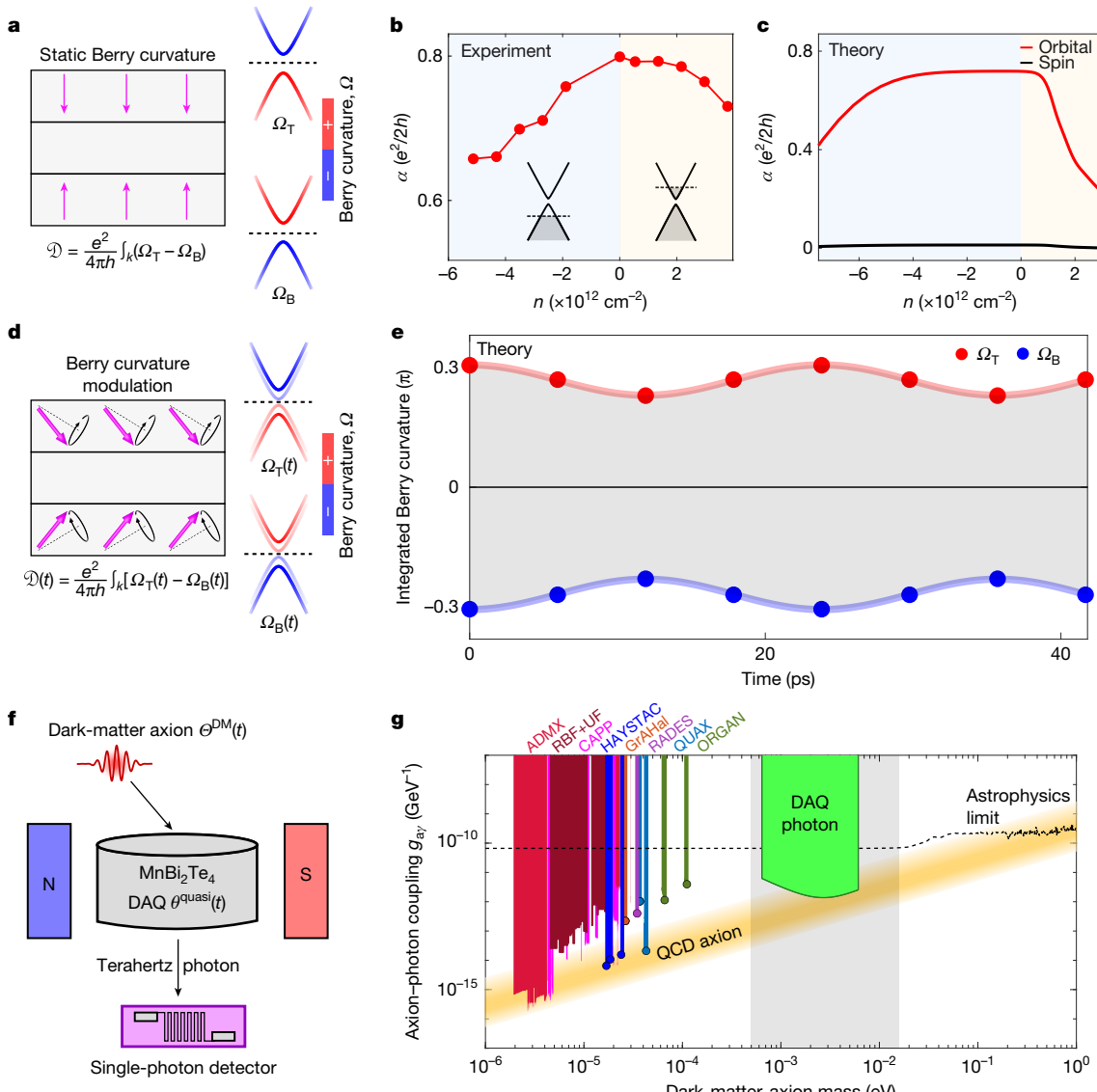


Fig. 4 | Ultrafast control of Berry curvature and dark-matter detection sensitivity. **a**, In 2D even-layer MnBi₂Te₄, the antiferromagnetic order generates opposite Berry curvatures on the top and bottom surfaces ($\Omega_T = -\Omega_B$), resulting in a Berry curvature real-space dipole \mathcal{D} . **b,c**, Experimentally measured (**b**) and theoretically calculated (**c**) static α as a function of carrier density n for six-layer MnBi₂Te₄. For theory, the orbital and spin contributions are computed separately (the insets illustrate the doping of the Dirac bands). **d**, The coherent precession of antiferromagnetic order potentially leads to an ultrafast control of Berry curvature. **e**, Calculated Berry curvature sum for the top and bottom surfaces at different spin angles for the out-of-phase magnons. The spin equilibrium angles are calculated based on the Heisenberg model (Supplementary Section I.2.1). The grey area corresponds to the Berry curvature real-space dipole \mathcal{D} . **f**, Schematic illustration of using the DAQ to

detect the dark-matter axions (θ^{DM} , the θ field of the dark matter axion).

g, Dark-matter detection sensitivity (g_{ax}) as a function of the axion mass. The mission is to search for the axion in the entire area that is below the horizontal dotted line (that is, the astrophysics limit). The microelectronvolt regime has been extensively explored. Each vertical coloured streak denotes a particular previous experiment (see ‘Estimation of the dark-matter-axon detection sensitivity’ in Methods). By contrast, the millielectronvolt regime (grey area) is particularly promising according to cosmology and astrophysics^{54,55}, but there is no detector. The yellow ribbon is the region where the dark-matter axion further solves the strong CP problem of quantum chromodynamics (QCD). The light green area shows the estimated detection range and sensitivity for the DAQ in MnBi₂Te₄.

Berry curvature origin

We now study the microscopic origin of α . We note that, independent of the microscopic origin, a coherent oscillation of θ always generates a DAQ. In other material candidates, the DAQ may arise from other mechanisms beyond Berry curvature (see discussion in the previous section).

The magnetoelectric coupling α has two contributions: spin and Berry curvature. The spin part comes from the localized magnetic ions (for example, 3d of Mn or Cr); the Berry curvature part comes from the orbital motion of itinerant electrons. Their relative contribution depends on the specific electronic structure of a system. To investigate

this in MnBi₂Te₄, we measure its static α as a function of the charge density n . Our data show that α varies with n (Fig. 4b). Importantly, changing n corresponds to changing the occupation of the itinerant electrons, whereas the localized Mn 3d orbitals are not affected. This can be clearly seen in the MnBi₂Te₄ band structure shown in Extended Data Fig. 5, where the Mn 3d bands are far (a few electronvolts) away from the Fermi energy. Therefore, the observed n dependence provides qualitative experimental evidence that the magnetoelectric coupling α in MnBi₂Te₄ is dominated by the orbital contribution from the itinerant electrons.

To achieve quantitative studies, we directly compute the different contributions of α based on the first-principles band structure of

six-layer MnBi_2Te_4 (Fig. 4c). Interestingly, the calculated Berry curvature contribution strongly dominates over the spin contribution, providing further supporting evidence. Moreover, the calculated n dependence show reasonable agreement with our experimental data. Therefore, we conclude that α in MnBi_2Te_4 is dominated by the orbital Berry curvature contribution. Specifically, this contribution equals the Berry curvature real-space dipole \mathcal{D} , for which we provide a band structure understanding as follows. A topological insulator features Dirac fermions on the top and bottom surfaces, which are gapped by the antiferromagnetic order, resulting in opposite Berry curvatures on opposite surfaces ($\Omega_T = -\Omega_B$). Hence, there is a Berry curvature real-space dipole $\mathcal{D} = \frac{e^2}{4\pi\hbar} \int_{\mathbf{k}} (\Omega_T - \Omega_B)$ (where \mathbf{k} is the wavevector in momentum space; see details in Fig. 4a). One can show from Berry phase theory that the orbital contribution of α equals \mathcal{D} (see derivation in 'α originating from Berry curvature real-space dipole \mathcal{D} ' in Methods).

We can now achieve further evidence for α equals \mathcal{D} . Even-layer MnBi_2Te_4 hosts an electric-field-induced anomalous Hall effect—the so-called layer Hall effect⁴⁸. This electrical transport Hall measurement, which is independent from the optical measurement above, provides another probe of \mathcal{D} . Specifically, one can show that the electric-field-induced anomalous Hall effect σ_{xy} measures $d\mathcal{D}/dn$ (derivation in Supplementary Information section IV). In addition, we obtain $d\alpha/dn$ by taking a derivative of our α data in Fig. 4b. As shown in Extended Data Fig. 3, the agreement between $d\mathcal{D}/dn$ and $d\alpha/dn$ further supports $\alpha = \mathcal{D}$, that is, the Berry curvature origin for the magneto-electric coupling in MnBi_2Te_4 .

Ultrafast control of Berry curvature by AFM magnon

Our experimental observation in Fig. 3c of ultrafast modulation of α naturally establishes an ultrafast modulation of Berry curvature real-space dipole because we showed $\alpha = \mathcal{D}$ above. To further confirm this, we directly compute the band structure at different spin angles of the magnon oscillation under the frozen magnon approximation. For the out-of-phase magnon, we see (Fig. 4e) that the top and bottom Berry curvatures oscillate with opposite phase. As such, their difference (grey area in Fig. 4e), which is the Berry curvature real-space dipole \mathcal{D} , also oscillates in time.

We can further try to understand why the in-phase magnon does not induce α oscillation. For the in-phase magnons, our calculation shows that the top and bottom Berry curvatures oscillate in time but with the same phase (Extended Data Fig. 6). So the Berry curvature real-space dipole \mathcal{D} is invariant in time. Therefore, the coherent oscillation of Berry curvature real-space dipole generates the DAQ in even-layer MnBi_2Te_4 .

We explain why the DAQ is strong in even-layered MnBi_2Te_4 . Beyond Berry curvature, it also requires hybridization between the top and bottom surface states owing to finite thickness. The strength of DAQ is measured by $\frac{\delta\theta}{\delta L_z}$ (ref. 6), that is, the change of θ per change of the antiferromagnetic order L_z . If we reduce the hybridization strength, θ becomes robust when L_z changes, leading to a small $\frac{\delta\theta}{\delta L_z}$. Only when the hybridization is comparable to the magnetism-induced Zeeman gap, a large $\frac{\delta\theta}{\delta L_z}$ is achieved. Our calculations in Extended Data Fig. 7 indeed shows that 6SL MnBi_2Te_4 is a good choice because of its large $\frac{\delta\theta}{\delta L_z}$. The thickness-dependent $\frac{\delta\theta}{\delta L_z}$ calculation also provides guidance on how the strength of the effect may evolve as a function of layer number.

Sensitivity of dark-matter-axion detection

Searching for the dark-matter axion is one of the most challenging yet exciting topics in fundamental physics. Below, we describe the state of the art in this field in terms of existing detectors and proposed future detectors and then estimate the axion detection frequency range and sensitivity based on our experimental results. This will justify why our DAQ approach can break new ground and make important

contributions. The axion mass is not known but astrophysics experiments have excluded mass > 1 eV. Therefore, the mission is to search for the axion below 1 eV, which is represented by the entire area below the horizontal dotted line (the astrophysics limit) in Fig. 4g. Given the vast frequency range, detectors should have tunable frequency. For example, the microelectronvolt regime, which corresponds to microwave frequencies, has been experimentally explored (vertical streaks in Fig. 4g), because microwave photon cavities with tunable frequencies can serve as the axion detectors in that regime.

By contrast, the millielectronvolt mass regime is particularly promising according to cosmology and astrophysics^{54,55} (grey region in Fig. 4g), but there is no axion detector for the millielectronvolt regime. This regime is more technologically challenging: cavity methods struggle, as tuning over wide ranges becomes difficult. As such, any detector in the millielectronvolt regime that goes below the astrophysics limit breaks new ground, and there are only two proposed future detectors known as BRASS and BREAD^{56,57}. Interestingly, theory^{21–23} predicts that the DAQ can serve as a detector in this regime (Fig. 4f). The basic working principle is explained in 'Estimation of the dark-matter-axion detection sensitivity' in Methods. A unique advantage is that the detection frequency can be continuously tuned over a wide range by $B_{||}$, because the detection frequency is given by $\sqrt{m_{\text{DAQ}}^2 + C^2 B_{||}^2}$, where $m_{\text{DAQ}} = 44$ GHz = 0.18 meV and C is a constant (see 'Estimation of the dark-matter-axion detection sensitivity' in Methods). However, this proposal has not been prominent in experimental particle physics as the DAQ remained a proposal. Going beyond the theory proposal^{21–23}, our work (1) provides realization of the DAQ, serving as an essential step forward, (2) makes the conceptional advance that the out-of-phase magnon under $B_{||}$ can effectively replace the antiferromagnetic amplitude mode; and (3) experimentally determines the DAQ frequency.

Using our experimental data and theoretical calculations, we calculate the DAQ sensitivity g_{av} in Fig. 4g (see Methods for details). The DAQ is able to go below astrophysical limit (the horizontal dotted line) over a wide frequency range, and even reach sensitivity to the quantum chromodynamics axion (yellow band in Fig. 4g) in a certain range. To build a well-functioning detector, more experimental studies and preparations are needed such as addressing the DAQ sample size issue and experimentally measuring the terahertz losses. We describe our solutions to these issues in 'Estimation of the dark-matter-axion detection sensitivity' in Methods and Supplementary Information section III.2. In Supplementary Information section III.3, we compare our DAQ approach with the other two proposed future detectors, BRASS and BREAD^{56,57}, and show that our approach has unique advantages.

DAQ materials beyond MnBi_2Te_4 and other outlooks

It is of interest to find other materials with a large DAQ. We need large but non-quantized θ that changes significantly upon a small change of the magnetic order. For example, although θ in Cr_2O_3 and Crl_3 are small, some multiferroics are reported to have large α , which are potentially promising for a large DAQ. The microscopic mechanism will be different, as the Berry curvature will be nearly zero in wide-gap insulators but there could be a large spin contribution.

Looking to the future, theory works^{6–23} have predicted a wide range of phenomena, such as the axion polariton⁶, the dynamical chiral magnetic effect¹⁵, finite momentum instability²⁰ and so on. In particular, the DAQ arises from magnetoelectric coupling and antiferromagnetic magnons, two phenomena of importance in spintronics. The observed coherent oscillation of $\alpha(t)$ means that a d.c. E field can control ultrafast spin polarization, $M(t) = \alpha(t)E$, which is potentially relevant to recent coherent antiferromagnetic spintronics²⁴. The coherent control of Berry curvature demonstrated here can be generalized. Berry curvature is only the imaginary part of quantum geometry, whereas the real part is the quantum metric, which has recently been observed in MnBi_2Te_4 (refs. 58,59). The magnons may be able to coherently

modulate its quantum metric, which can be detected by measuring the nonlinear Hall effect with time resolution. Beyond MnBi_2Te_4 , in magnetic Weyl semimetals such as $\text{Co}_3\text{Sn}_2\text{S}_2$ or Mn_3Sn , the magnetic spin direction dictates the k -space locations of the Weyl nodes. The magnons may coherently control the Weyl node locations, leading to a time-dependent anomalous Hall effect. Finally, nonlinearly driven magnons⁶⁰ may induce new non-equilibrium phases in analogy to the light-induced superconductivity driven by phonons²⁶.

Online content

Any methods, additional references, Nature Portfolio reporting summaries, source data, extended data, supplementary information, acknowledgements, peer review information; details of author contributions and competing interests; and statements of data and code availability are available at <https://doi.org/10.1038/s41586-025-08862-x>.

1. Wilczek, F. Problem of strong \mathcal{P} and \mathcal{P} invariance in the presence of instantons. *Phys. Rev. Lett.* **40**, 279–282 (1978).
2. Weinberg, S. A new light boson? *Phys. Rev. Lett.* **40**, 223–226 (1978).
3. Essin, A. M., Moore, J. E. & Vanderbilt, D. Magnetoelectric polarizability and axion electrodynamics in crystalline insulators. *Phys. Rev. Lett.* **102**, 146805 (2009).
4. Wu, L. et al. Quantized Faraday and Kerr rotation and axion electrodynamics of a 3D topological insulator. *Science* **354**, 1124–1127 (2016).
5. Mogi, M. et al. Experimental signature of the parity anomaly in a semi-magnetic topological insulator. *Nat. Phys.* **18**, 390–394 (2022).
6. Li, R., Wang, J., Qi, X.-L. & Zhang, S.-C. Dynamical axion field in topological magnetic insulators. *Nat. Phys.* **6**, 284–288 (2010).
7. Wang, J., Lei, C., MacDonald, A. H. & Binek, C. Dynamic axion field in the magnetoelectric antiferromagnet chromia. Preprint at <https://arxiv.org/abs/1901.08536> (2019).
8. Zhang, J. et al. Large dynamical axion field in topological antiferromagnetic insulator MnBi_2Te_3 . *Chin. Phys. Lett.* **37**, 077304 (2020).
9. Wang, H. et al. Dynamical axion state with hidden pseudospin Chern numbers in MnBi_2Te_4 -based heterostructures. *Phys. Rev. B* **101**, 081109 (2020).
10. Zhu, T., Wang, H., Zhang, H. & Xing, D. Tunable dynamical magnetoelectric effect in antiferromagnetic topological insulator MnBi_2Te_4 films. *npj Comput. Mater.* **7**, 121 (2021).
11. Røising, H. S. et al. Axion–matter coupling in multiferroics. *Phys. Rev. Res.* **3**, 033236 (2021).
12. Liu, Z., Xiao, J. & Wang, J. Dynamical magnetoelectric coupling in axion insulator thin films. *Phys. Rev. B* **105**, 214424 (2022).
13. Lhachemi, M. N. Y. & Garate, I. Phononic dynamical axion in magnetic Dirac insulators. *Phys. Rev. B* **109**, 144304 (2024).
14. Shiozaki, K. & Fujimoto, S. Dynamical axion in topological superconductors and superfluids. *Phys. Rev. B* **89**, 054506 (2014).
15. Sekine, A. & Nomura, K. Chiral magnetic effect and anomalous Hall effect in antiferromagnetic insulators with spin–orbit coupling. *Phys. Rev. Lett.* **116**, 096401 (2016).
16. Sekine, A. & Chiba, T. Electric-field-induced antiferromagnetic resonance in antiferromagnetic insulators with spin–orbit coupling. *AIP Adv.* **7**, 055902 (2017).
17. Taguchi, K. et al. Electromagnetic effects induced by a time-dependent axion field. *Phys. Rev. B* **97**, 214409 (2018).
18. Terças, H., Rodrigues, J. & Mendonça, J. Axion-plasmon polaritons in strongly magnetized plasmas. *Phys. Rev. Lett.* **120**, 181803 (2018).
19. Xiao, Y. et al. Nonlinear level attraction of cavity axion polariton in antiferromagnetic topological insulator. *Phys. Rev. B* **104**, 115147 (2021).
20. Curtis, J. B., Petrides, I. & Narang, P. Finite-momentum instability of a dynamical axion insulator. *Phys. Rev. B* **107**, 205118 (2023).
21. Marsh, D. J., Fong, K. C., Lentz, E. W., Smekal, L. & Ali, M. N. Proposal to detect dark matter using axionic topological antiferromagnets. *Phys. Rev. Lett.* **123**, 121601 (2019).
22. Schütte-Engel, J. et al. Axion quasiparticles for axion dark matter detection. *J. Cosmol. Astropart. Phys.* **2021**, 066 (2021).
23. Chigusa, S., Moroi, T. & Nakayama, K. Axion/hidden-photon dark matter conversion into condensed matter axion. *J. High Energy Phys.* **2021**, 1–33 (2021).
24. Han, J., Cheng, R., Liu, L., Ohno, H. & Fukami, S. Coherent antiferromagnetic spintronics. *Nat. Mater.* **22**, 684–695 (2023).
25. De La Torre, A. et al. Nonthermal pathways to ultrafast control in quantum materials. *Rev. Mod. Phys.* **93**, 041002 (2021).
26. Mitrano, M. et al. Possible light-induced superconductivity in K_3C_{60} at high temperature. *Nature* **530**, 461–464 (2016).
27. Sie, E. J. et al. An ultrafast symmetry switch in a Weyl semimetal. *Nature* **565**, 61–66 (2019).
28. Bae, Y. J. et al. Exciton-coupled coherent magnons in a 2D semiconductor. *Nature* **609**, 282–286 (2022).
29. Gao, F. Y. et al. Giant chiral magnetoelectric oscillations in a van der Waals multiferroic. *Nature* **632**, 273–279 (2024).
30. Kiriyuk, A., Kimel, A. V. & Rasing, T. Ultrafast optical manipulation of magnetic order. *Rev. Mod. Phys.* **82**, 2731–2784 (2010).
31. Allen, M. et al. Visualization of an axion insulating state at the transition between 2 chiral quantum anomalous Hall states. *Proc. Natl. Acad. Sci. USA* **116**, 14511–14515 (2019).
32. Gooth, J. et al. Axionic charge-density wave in the Weyl semimetal $(\text{TaSe}_4)_2$. *Nature* **575**, 315–319 (2019).
33. Sinchenko, A. A., Ballou, R., Lorenzo, J. E., Grenet, T. & Monceau, P. Does $(\text{TaSe}_4)_2$ really harbor an axionic charge density wave? *Appl. Phys. Lett.* **120**, 063102 (2022).
34. Bartram, F. M. et al. Ultrafast coherent interlayer phonon dynamics in atomically thin layers of MnBi_2Te_4 . *npj Quantum Mater.* **7**, 84 (2022).
35. Lujan, D. et al. Magnons and magnetic fluctuations in atomically thin MnBi_2Te_4 . *Nat. Commun.* **13**, 2527 (2022).
36. Bartram, F. M. et al. Real-time observation of magnetization and magnon dynamics in a two-dimensional topological antiferromagnet MnBi_2Te_4 . *Sci. Bull.* **68**, 2734–2742 (2023).
37. Padmanabhan, H. et al. Large exchange coupling between localized spins and topological bands in MnBi_2Te_4 . *Adv. Mater.* **34**, 2202841 (2022).
38. Padmanabhan, H. et al. Interlayer magnetophononic coupling in MnBi_2Te_4 . *Nat. Commun.* **13**, 1929 (2022).
39. Cheng, L., Xiang, T. & Qi, J. Magnetic-order-mediated carrier and phonon dynamics in MnBi_2Te_4 . *Phys. Rev. Res.* **6**, 023073 (2024).
40. Qiu, J.-X. et al. Axion optical induction of antiferromagnetic order. *Nat. Mater.* **22**, 583–590 (2023).
41. Otrokov, M. M. et al. Prediction and observation of an antiferromagnetic topological insulator. *Nature* **576**, 416–422 (2019).
42. Li, J. et al. Intrinsic magnetic topological insulators in van der Waals layered MnBi_2Te_4 family materials. *Sci. Adv.* **5**, eaaw5685 (2019).
43. Zhang, D. et al. Topological axion states in the magnetic insulator MnBi_2Te_4 with the quantized magnetoelectric effect. *Phys. Rev. Lett.* **122**, 206401 (2019).
44. Deng, Y. et al. Quantum anomalous Hall effect in intrinsic magnetic topological insulator MnBi_2Te_4 . *Science* **367**, 895–900 (2020).
45. Liu, C. et al. Robust axion insulator and Chern insulator phases in a two-dimensional antiferromagnetic topological insulator. *Nat. Mater.* **19**, 522–527 (2020).
46. Yang, S. et al. Odd-even layer-number effect and layer-dependent magnetic phase diagrams in MnBi_2Te_4 . *Phys. Rev. X* **11**, 011003 (2021).
47. Ovchinnikov, D. et al. Intertwined topological and magnetic orders in atomically thin Chern insulator MnBi_2Te_4 . *Nano Lett.* **21**, 2544–2550 (2021).
48. Gao, A. et al. Layer Hall effect in a 2D topological axion antiferromagnet. *Nature* **595**, 521–525 (2021).
49. Cao, T., Shao, D.-F., Huang, K., Gurung, G. & Tsymbal, E. Y. Switchable anomalous Hall effects in polar-stacked 2D antiferromagnet MnBi_2Te_4 . *Nano Lett.* **23**, 3781–3787 (2023).
50. Li, Y. et al. Fabrication-induced even-odd discrepancy of magnetotransport in few-layer MnBi_2Te_4 . *Nat. Commun.* **15**, 3399 (2024).
51. Chong, S. K. et al. Intrinsic exchange biased anomalous Hall effect in an uncompensated antiferromagnet MnBi_2Te_4 . *Nat. Commun.* **15**, 2881 (2024).
52. Fonseca, J. et al. Picosecond ultrasonics in magnetic topological insulator MnBi_2Te_4 . *Nano Lett.* **24**, 10562–10568 (2024).
53. Zhang, X.-X. et al. Gate-tunable spin waves in antiferromagnetic atomic bilayers. *Nat. Mater.* **19**, 838–842 (2020).
54. Gorghetto, M., Hardy, E. & Villadoro, G. More axions from strings. *SciPost Phys.* **10**, 050 (2021).
55. Saikawa, K., Redondo, J., Vaquero, A. & Kaltschmidt, M. Spectrum of global string networks and the axion dark matter mass. *J. Cosmol. Astropart. Phys.* **2024**, 043 (2024).
56. Horns, D. et al. Searching for WISPy cold dark matter with a dish antenna. *J. Cosmol. Astropart. Phys.* **2013**, 016 (2013).
57. Liu, J. et al. Broadband solenoidal haloscope for terahertz axion detection. *Phys. Rev. Lett.* **128**, 131801 (2022).
58. Wang, N. et al. Quantum-metric-induced nonlinear transport in a topological antiferromagnet. *Nature* **621**, 487–492 (2023).
59. Gao, A. et al. Quantum metric nonlinear Hall effect in a topological antiferromagnetic heterostructure. *Science* **381**, 181–186 (2023).
60. Zhang, Z. et al. Terahertz-field-driven magnon upconversion in an antiferromagnet. *Nat. Phys.* **20**, 788–793 (2024).

Publisher's note Springer Nature remains neutral with regard to jurisdictional claims in published maps and institutional affiliations.

Springer Nature or its licensor (e.g. a society or other partner) holds exclusive rights to this article under a publishing agreement with the author(s) or other rightsholder(s); author self-archiving of the accepted manuscript version of this article is solely governed by the terms of such publishing agreement and applicable law.

© The Author(s), under exclusive licence to Springer Nature Limited 2025

Methods

Bulk crystal growth and 2D sample fabrication

Our MnBi_2Te_4 bulk crystals were grown using the Bi_2Te_3 flux method⁶¹. Elemental Mn, Bi and Te were mixed at a molar ratio of 15:170:270, loaded in a crucible, and sealed in a quartz tube under one-third atmospheric pressure of argon. The ampule was first heated to 900 °C for 5 h. It was then moved to another furnace where it slowly cooled from 597 °C to 587 °C and stayed at 587 °C for 1 day. The 2D device fabrication processes were completed in an argon environment without exposure to air, chemicals, or heat (oxygen and water level below 0.01 ppm and a dew point below -96 °C). The glovebox was attached to an e-beam evaporator, allowing us to make metal deposition without exposure to air. MnBi_2Te_4 was mechanically exfoliated onto a baked 300-nm silicon dioxide/silicon wafer using Scotch tape. A stencil mask technique⁴⁸ was used to make chromium/gold contacts on top of MnBi_2Te_4 . Boron nitride (BN) flakes were directly exfoliated onto a polydimethylsiloxane film, and a 10–30-nm-thick BN flake was identified and transferred onto the MnBi_2Te_4 as the top gate dielectric layer. Next, a metal gate was evaporated onto the BN/ MnBi_2Te_4 heterostructure. Supplementary Information section I.3 presents additional measurements to assess the sample quality following the processing of the electric contacts.

How we characterized the magnon frequencies

We followed the experimental methods in refs. 53,62, which measured the magnon frequencies in bilayer CrI_3 , also a fully compensated layered antiferromagnet. In this method, monolayer WSe_2 is stacked on top of the layered antiferromagnet (Extended Data Fig. 1e). This monolayer WSe_2 breaks the layer degeneracy, allowing us to selectively probe the top-layer information^{53,62}. Pump–probe Kerr rotation under normal incidence was performed on this heterostructure. The pump laser launches the magnons. The probe Kerr rotation measures the out-of-plane magnetization M_z of the top layer preferentially because of the WSe_2 . The data are shown in Extended Data Fig. 1f,g. Coherent oscillations composed of two distinct frequencies are clearly observed, corresponding to the in-phase and the out-of-phase magnons. The monolayer WSe_2 allows us to selectively probe the top layer, which is crucial for observing both modes. We emphasize that the monolayer WSe_2 is only used in this dataset (Extended Data Fig. 1) to characterize the magnon frequencies. For all other measurements (everything in the main text), we used even-layer MnBi_2Te_4 without WSe_2 . Additional pump photon polarization dependence (Supplementary Information section I.2) shows that the excitation mechanism is laser-heating-induced coherent precession. In future, one way to selectively excite the in-phase and out-of-phase magnons may be to use microwave/terahertz photons that are resonant with the corresponding magnon polariton frequencies.

The femtosecond laser pulse was generated by an amplified ytterbium-doped potassium gadolinium tungstate (Yb:KGW) laser (Pharos, LightConversion) with a pulse duration of 168 fs, a wavelength of 1,030 nm and a repetition rate of 100 kHz. For the pump beam, an optical parametric amplifier (Orpheus, LightConversion) was used to tune the wavelength to 720 nm (pump fluence of about 3 $\mu\text{J cm}^{-2}$). For the probe beam, a beta-barium borate (BBO) crystal was used to convert the laser wavelength to 515 nm. The pump beam went through an optical chopper at 1,000 Hz and was combined with the probe beam by a dichroic mirror, both of which were focused on the sample (spot size about 1 μm). The reflected beam was filtered to remove the pump beam, passed through a half-wave plate and a Wollaston prism, and entered the balanced photodiode detector. The balanced photodiode signal was analysed by a lock-in amplifier at the chopper frequency.

How we converted α to the unit of $e^2/2h$

The antiferromagnetic ground state of even-layer MnBi_2Te_4 features magnetoelectric coupling, which is the electric-field-induced magnetization $\alpha = \frac{dM}{dE}$. The out-of-plane electric field E_z was applied by the

top and bottom gates; the net out-of-plane magnetization M_z was probed by the optical Kerr rotation under normal incidence⁶³, Kerr rotation = M_z/γ (γ is a material-specific conversion coefficient). Therefore, we have $\alpha = \gamma \frac{\text{dKerr rotation}}{\text{d}E_z}$. To convert α from the directly measured unit of $\mu\text{rad V}^{-1} \text{nm}$ to the unit of $e^2/2h$, we need to determine the coefficient γ .

We (semi-)quantitatively determined γ using a method reported in ref. 64. This method uses the fact that the magnetic order of MnBi_2Te_4 can be controlled by the out-of-plane magnetic field B_\perp . With increasing B_\perp , the magnetic order changes from the layered antiferromagnetic state to a spin-flop state. In the spin-flop state at $B_\perp = 6$ T, we measured both the Kerr rotation and the M_z , from which we determined the value of γ (Extended Data Fig. 4). Using this γ , we converted the α of the antiferromagnetic state to the unit of $e^2/2h$. In this method, we needed to assume that the spin-flop state at $B_\perp = 6$ T and the antiferromagnetic state at $B_\perp = 0$ T have the same γ . This is an approximation.

How we measured the DAQ

The DAQ manifests as a coherent oscillation of the magnetoelectric coupling, which requires us to measure $\alpha(t)$ with femtosecond time resolution. This was achieved by combining ultrafast pump–probe optics with 2D electronic devices. We built a dual-gated six-layer MnBi_2Te_4 device (no WSe_2). The probe beam combined with the gate-applied E_z measures α , whereas the pump beam excites the magnons. By varying the delay time t , we can measure $\alpha(t)$ with femtosecond time resolution.

Experimentally, this was achieved by connecting two lock-in amplifiers in series as illustrated in Extended Data Fig. 2a. An optical chopper modulated the pump laser at frequency $\omega_1 = 1,000$ Hz. A functional generator modulated the electric field at frequency $\omega_2 = 0.7$ Hz and with a.c. modulation amplitude $\Delta E = 0.84$ V nm^{-1} . The signal collected by the balanced photodiode detector was first fed into a lock-in at the chopper frequency $\omega_1 = 1,000$ Hz and then into the second lock-in at the functional generator (E_z) frequency $\omega_2 = 0.7$ Hz. We used the fundamental beam of our Yb:KGW laser as the pump (1,030 nm and fluence is about 160 $\mu\text{J cm}^{-2}$) and its second harmonic as the probe (515 nm). For the static MOKE measurement in Fig. 2, the probe wavelength was also set to 515 nm. Supplementary Information section I.3 shows the photon-energy dependence, confirming that the specific choice of photon energy does not affect our conclusion.

α originating from Berry curvature real-space dipole \mathcal{D}

In a \mathcal{PT} -symmetric material, the magnetoelectric coupling α manifests as an electric-field E_z -induced magnetization. Here we focus on the orbital contribution of α , so $\alpha^{\text{orb.}} = \frac{M_z^{\text{orb.}}}{E_z}$. According to refs. 65–67, the orbital magnetization $M_z^{\text{orb.}}$ of a quasi-2D system with thickness d is given by

$$M_z^{\text{orb.}} = \frac{e}{\hbar d} \text{Im} \sum_n \int_{\epsilon_{nk} \leq \mu} \frac{dk_x dk_y}{(2\pi)^2} \langle \partial_{k_x} u_{nk} | H_k + \epsilon_{nk} - 2\mu | \partial_{k_y} u_{nk} \rangle,$$

In the equation above, \hbar is the reduced Planck constant, μ is the chemical potential, and u_{nk} is the periodic part of the Bloch wavefunction for the n th band. Therefore, we have^{67,68}

$$\frac{\partial M^z}{\partial \mu} = \frac{e}{\hbar d} \frac{1}{2\pi} \sum_n \int_{\epsilon_{nk} \leq \mu} dk_x dk_y \Omega_n, \quad (1)$$

Here we have utilized the fact that the Berry curvature $\Omega_n = -2\text{Im} \langle \partial_{k_x} u_{nk} | \partial_{k_y} u_{nk} \rangle$. As the Berry curvature vanishes inside the bulk, we can focus on the surface degrees of freedom.

Under a uniform vertical electric field E_z , the chemical potentials for the top (T) and bottom (B) surfaces change by $\delta(\mu^T - \mu^B) = E_z d$, such that for the total out-of-plane orbital magnetization $M_z^{\text{orb.}} = M_z^{\text{T,orb.}} + M_z^{\text{B,orb.}}$ changes by

Article

$$\alpha_{zz} \equiv \frac{\partial M_z^{\text{orb.}}}{\partial E_z} = \frac{\partial M_z^{\text{T,orb.}}}{\partial E_z} + \frac{\partial M_z^{\text{B,orb.}}}{\partial E_z} = \frac{\partial M_z^{\text{T,orb.}}}{\partial \mu^{\text{T}}} \frac{\partial \mu^{\text{T}}}{\partial E_z} + \frac{\partial M_z^{\text{B,orb.}}}{\partial \mu^{\text{B}}} \frac{\partial \mu^{\text{B}}}{\partial E_z}$$

We then can rewrite μ^{T} and μ^{B} as $\frac{\mu^{\text{T}} + \mu^{\text{B}}}{2} + \frac{\mu^{\text{T}} - \mu^{\text{B}}}{2}$ and $\frac{\mu^{\text{T}} + \mu^{\text{B}}}{2} - \frac{\mu^{\text{T}} - \mu^{\text{B}}}{2}$, respectively. Then, we have:

$$\begin{aligned} \alpha_{zz} &= \frac{1}{2} \left(\frac{\partial M_z^{\text{T,orb.}}}{\partial \mu^{\text{T}}} + \frac{\partial M_z^{\text{B,orb.}}}{\partial \mu^{\text{B}}} \right) \frac{\partial (\mu^{\text{T}} + \mu^{\text{B}})}{\partial E_z} \\ &\quad + \frac{1}{2} \left(\frac{\partial M_z^{\text{T,orb.}}}{\partial \mu^{\text{T}}} - \frac{\partial M_z^{\text{B,orb.}}}{\partial \mu^{\text{B}}} \right) \frac{\partial (\mu^{\text{T}} - \mu^{\text{B}})}{\partial E_z} \end{aligned}$$

Owing to \mathcal{PT} symmetry, we have $\frac{\partial M_z^{\text{T,orb.}}}{\partial \mu^{\text{T}}} + \frac{\partial M_z^{\text{B,orb.}}}{\partial \mu^{\text{B}}} = 0$. Also, we know that $\frac{\partial (\mu^{\text{T}} - \mu^{\text{B}})}{\partial E_z} = ed$. As such, we can get

$$\alpha_{zz} = \frac{ed}{2} \left(\frac{\partial M_z^{\text{T,orb.}}}{\partial \mu^{\text{T}}} - \frac{\partial M_z^{\text{B,orb.}}}{\partial \mu^{\text{B}}} \right) \quad (2)$$

Plugging equation (1) into equation (2), we get

$$\alpha_{zz} = \frac{e^2}{2h} \frac{1}{2\pi} \sum_n \int_{\varepsilon_{nk} \leq \mu} dk_x dk_y (\Omega_n^{\text{T}} - \Omega_n^{\text{B}}) = \mathcal{D} \quad (3)$$

Estimation of the dark-matter-axion detection sensitivity

Detection scheme 1 (photon counting). In the presence of external magnetic field $B_{||}$, the dark-matter (DM) axion of mass m_{DM} can be converted into a photon at the same energy. In the DAQ material, that terahertz photon and the DAQ can resonantly couple to form a DAQ polariton⁶. The resonant interaction leads to enhanced electromagnetic signals (that is, photon amplification)^{21,22,69,70}, which are eventually emitted off the DAQ material and detected by a single-photon detector (Fig. 4f). Moreover, resonant frequency between the DAQ and the photon can be directly controlled by the external $B_{||}$ field, given by $\omega_{\text{resonance}} = \sqrt{m_{\text{DAQ}}^2 + b^2}$, where $b = \frac{e^2}{2\sqrt{2}\epsilon_0 f_\theta} B_{||}$. m_{DAQ} is the DAQ mass, which is about 44 GHz in our materials, ϵ_0 and ϵ are the permittivity of vacuum and of the material, and $f_\theta = 82$ eV for our material. The small correction $\delta\omega_j^2$ (see equation (4.33) in ref. 22) is negligible, as shown in Supplementary Information section III.1.

Sensitivity estimation. The detection sensitivity g_{ay} based on photon counting is shown in Fig. 4g. g_{ay} is given by²²

$$g_{ay} = \frac{m_{\text{DM}}^{3/2}}{B_{||} \beta \sqrt{S \eta \rho_{\text{DM}}}} \sqrt{\frac{1}{\tau} + 2 \sqrt{\frac{\lambda_d}{\tau}}}$$

In the expression above, $\rho_{\text{DM}} \approx 0.4 \text{ GeV cm}^{-3}$ is the local axion dark-matter density. τ is the measurement time at a specific magnetic field, which was on the order of minutes to scan 1 decade in axion dark-matter mass if the total experimental run time is 3 years. η is the detection efficiency of the terahertz single-photon detector (set to 95%). λ_d is the dark-count rate of the photon detector (set to 10^{-5}). S is the sample area, which was set to 0.16 m^2 . β is the boost factor, which was estimated to be 100 in our material using the following expression, $\beta = \frac{4}{\frac{4\pi^2}{m_{\text{DM}}^2 d^2} + \left(\frac{m_{\text{DM}}^2 f_m}{b^2} + \Gamma_p \right) dn^2}$. Here n is the dielectric constant of the mate-

rial (about 6.4) and d is the thickness of the material (we assumed an optimal thickness of 0.4 mm). f_m is the magnetic impurity density, which is estimated to be 0.7×10^{-3} . Γ_p is the imaginary part of the dielectric constant at the frequency of m_{DM} (about 0.2×10^{-3}). Supplementary Information section III details how we estimated the values of the parameters above based on our experimental and theoretical results.

We also note that in Fig. 4g, each vertical streak denotes a particular previous experiments (data extracted from ref. 71).

Future experimental preparations are needed to actually build a functional detector. For example, this photon-counting approach requires a large sample with optimal thickness about 0.4 mm. However, the DAQ in six-layer MnBi₂Te₄ relies on finite-thickness hybridization. Supplementary Information section III describes our proposed future works to address all issues, including sample size and terahertz single-photon detectors. For example, we propose to grow thick samples that consist of a repeating superlattice between six-layer MnBi₂Te₄ and the spacer layer.

Detection scheme 2 (Kerr). We propose a different detection approach that does not need a thick sample. Although this approach is less sensitive (Extended Data Fig. 8), it serves as a first step that is readily applicable to our existing six-layer MnBi₂Te₄. Meanwhile, we address the sample thickness issue (Supplementary Information section III.2). This Kerr method is very similar to the experiments in the main text, but replace the pump laser (visible photons) by the dark-matter axion. In the presence of a $B_{||}$ field, the dark-matter axion can be converted into a millielectronvolt (subterahertz) photon, and that photon and the DAQ can resonantly couple to form an axion polariton, which is essentially a coherent oscillation of $\theta(\omega)$, where $\omega = \sqrt{m_{\text{DAQ}}^2 + b^2}$. By applying an out-of-plane electric field E_z , such a coherent oscillation of $\theta(\omega)$ will lead to an oscillating magnetization $M_z(\omega) = \theta(\omega)E_z$. We propose to use MOKE with start-of-the-art sensitivity to measure this oscillating magnetization. In this way, the sample size is not an issue, because Kerr measures the magnetization, which is per volume.

Sensitivity estimation. The sensitivity g_{ay} of this approach is shown in Extended Data Fig. 8. g_{ay} can be expressed by

$$g_{ay} = \frac{2hy S_{\text{Kerr}} f_\theta m_{\text{DM}} m_{\text{DAQ}} \Gamma_m}{e^2 E_z B_{||} \sqrt{2\tau_{\text{Kerr}} \rho_{\text{DM}}}}$$

Here E_z is the applied electric field, for which we use a value of 2 V nm^{-1} . y is the conversion factor between Kerr rotation and magnetization, which is estimated as $1.4 \times 10^4 \text{ A m}^{-1} \text{ rad}^{-1}$ in the best-case scenario⁷². S_{Kerr} is the sensitivity for Kerr rotation measurement, which is estimated to be $0.7 \text{ nrad}/\sqrt{\text{Hz}}$ under a.c. modulation⁷³. h is the Planck constant and e is the electron charge. τ_{Kerr} is the measurement time for Kerr rotation, which is estimated to be 3 months. It is noted that ρ_{DM} , Γ_m , m_{DAQ} , f_θ , m_{DM} and $B_{||}$ have been defined and estimated in the previous section.

Electronic-structure calculations. First-principles calculations were performed using the projector-augmented-wave method as implemented in the Vienna ab initio simulation package (VASP). To simulate thin-film MnBi₂Te₄, a $9 \times 9 \times 1$ Γ -centred k -grid was used for the Brillouin zone integration, and the kinetic energy cut-off was set to 400 eV. The exchange-correlation was approximated within the generalized gradient approximation (GGA) framework. The Wannier models of MnBi₂Te₄ were built using Mn *d*, Bi *p* and Te *p* orbitals. On-site Coulomb potentials of $U = 5$ eV for Mn *d* were applied. We also used the tight-binding model for six-layer MnBi₂Te₄ (see Supplementary Information section V for details), which was described in ref. 74. Each layer contained two orbitals and two spins (four bands) and different layers were coupled with symmetry-allowed interlayer hybridization. The antiferromagnetic order was described by a layer-dependent Zeeman energy.

The θ is the trace part of the magnetoelectric coupling α .

$$\theta = \pi \frac{2h}{3e^2} \sum_{i=x,y,z} \alpha_{ii} \quad (4)$$

We note that the above expression only holds only when the Dirac surface states are gapped by magnetic order. In the presence of perfect

time-reversal symmetry both in the bulk and on the surface of a sample, α is zero irrespective of the topological nature. We also note that in the main text, we assumed that α is isotropic $\alpha_{xx} = \alpha_{yy} = \alpha_{zz}$, so that $\theta = \pi \frac{2\hbar}{e^2} \alpha$. This is a good approximation for MnBi_2Te_4 but not necessarily true for other materials. α_{ii} was directly computed from the electronic structure by the following expressions

$$\alpha_{xx} = \frac{e^2}{V} \sum_{m,n} \int \frac{f_n - f_m}{\varepsilon_m - \varepsilon_n} \text{Re} \left[r_{nm}^x \langle m(\mathbf{k}) | -\frac{1}{2} (\hat{v}^y \hat{r}^z + \hat{r}^z \hat{v}^y) + m_e^{-1} \hat{S}_x | n(\mathbf{k}) \rangle \right], \quad (5)$$

$$\alpha_{yy} = \frac{e^2}{V} \sum_{m,n} \int \frac{f_n - f_m}{\varepsilon_m - \varepsilon_n} \text{Re} \left[r_{nm}^y \langle m(\mathbf{k}) | \frac{1}{2} (\hat{v}^x \hat{r}^z + \hat{r}^z \hat{v}^x) + m_e^{-1} \hat{S}_y | n(\mathbf{k}) \rangle \right], \quad (6)$$

$$\begin{aligned} \alpha_{zz} = & \frac{e^2}{V} \sum_{m,n} \int \frac{f_n - f_m}{\varepsilon_m - \varepsilon_n} \text{Re} \left[\frac{1}{2} \sum_{p: \varepsilon_p \neq \varepsilon_m} (r_{nm}^z r_{mp}^x v_{pn}^y - r_{np}^z r_{pm}^x v_{mn}^y \right. \\ & \left. + r_{nm}^z r_{mn}^x v_{mm}^y - (x \leftrightarrow y)) + r_{mn}^z m_e^{-1} (\hat{S}_z)_{mn} \right], \end{aligned} \quad (7)$$

In the equations above, m, n are the band indices, $\int = \int dk_x dk_y / (2\pi)^2$, f_n is the Fermi Dirac function with energy ε_n of band n , \hat{r} and \hat{v} are the position and velocity and spin operators, and m_e is the electron mass. As explained in the main text, α has two microscopic contributions, spin and orbital. The last term of each equation, related to the spin operator \hat{S} , accounts for the spin contribution; the other terms account for the orbital contribution. We note that the expressions above are valid when the Fermi level is inside the bandgap, which is true for all experiments except the carrier density dependence in Fig. 4b,c. When the Fermi level cuts into the band, α_{zz} has an additional Fermi surface contribution term $\frac{e^2}{V} \sum_n \int \frac{\partial f_n}{\partial \varepsilon_n} \frac{1}{2} (v_n^y g_n^{zx} - v_n^x g_n^{zy})$, where $g_n^{ij} = \text{Re}[\sum_m r_{nm}^i r_{mn}^j]$ is the quantum metric of band n .

The Berry curvature real-space dipole \mathcal{D} is

$$\mathcal{D} = \frac{e^2}{4\pi\hbar} \sum_n \left(\int_{\varepsilon_n \leq \mu} \Omega_n^T - \int_{\varepsilon_n \leq \mu} \Omega_n^B \right) \quad (8)$$

$\Omega_n^{T(B)}$ is the layer-resolved Berry curvature of the n th band as defined in ref. 75 (T and B indicate the top and bottom surface, respectively), which is given by

$$\Omega_n^{T(B)} = -2\text{Im} \sum_{m,n'} \frac{\langle n(\mathbf{k}) | v_x | m(\mathbf{k}) \rangle \langle m(\mathbf{k}) | v_y | n'(\mathbf{k}) \rangle}{(\varepsilon_m - \varepsilon_n)^2} \rho_{nn'}^{T(B)}(\mathbf{k}) \quad (9)$$

where $\rho_{nn'}^{T(B)}(\mathbf{k}) = \sum_{j \in T(B)} \langle n(\mathbf{k}) | j \rangle \langle j | n'(\mathbf{k}) \rangle$ describes the projection on to the top or bottom layer.

Data availability

All data that support the findings of this study are available from the corresponding author on request. Source data are provided with this paper.

61. Yan, J.-Q. et al. Crystal growth and magnetic structure of MnBi_2Te_4 . *Phys. Rev. Mater.* **3**, 064202 (2019).
62. Zhong, D. et al. Layer-resolved magnetic proximity effect in van der Waals heterostructures. *Nat. Nanotechnol.* **15**, 187–191 (2020).
63. Huang, B. et al. Layer-dependent ferromagnetism in a van der Waals crystal down to the monolayer limit. *Nature* **546**, 270–273 (2017).
64. Jiang, S., Shan, J. & Mak, K. F. Electric-field switching of two-dimensional van der Waals magnets. *Nat. Mater.* **17**, 406–410 (2018).
65. Xiao, D., Shi, J. & Niu, Q. Berry phase correction to electron density of states in solids. *Phys. Rev. Lett.* **95**, 137204 (2005).
66. Thonhauser, T., Ceresoli, D., Vanderbilt, D. & Resta, R. Orbital magnetization in periodic insulators. *Phys. Rev. Lett.* **95**, 137205 (2005).

67. Ceresoli, D., Thonhauser, T., Vanderbilt, D. & Resta, R. Orbital magnetization in crystalline solids: multi-band insulators, Chern insulators, and metals. *Phys. Rev. B* **74**, 024408 (2006).
68. Raffaele, B. & Raffaele, R. Orbital magnetization in insulators: bulk versus surface. *Phys. Rev. B* **93**, 174417 (2016).
69. Chadha-Day, F., Ellis, J. & Marsh, D. J. E. Axion dark matter: what is it and why now? *Sci. Adv.* **8**, eabj3618 (2022).
70. Srivcek, P. & Witten, E. Axions in string theory. *J. High Energy Phys.* **2006**, 051 (2006).
71. O'Hare, C. cajohare/axionLimits:AxionLimits. GitHub <https://cajohare.github.io/AxionLimits/> (2020).
72. Tao, Z. et al. Valley-coherent quantum anomalous Hall state in AB-stacked $\text{MoTe}_2/\text{WSe}_2$ bilayers. *Phys. Rev. X* **14**, 011004 (2024).
73. Ma, J. et al. Improving the sensitivity of DC magneto-optical Kerr effect measurement to 10^{-7} rad./ $\sqrt{\text{Hz}}$. *Chin. Opt. Lett.* **20**, 111201 (2022).
74. Liu, Z. & Wang, J. Anisotropic topological magnetoelectric effect in axion insulators. *Phys. Rev. B* **101**, 205130 (2020).
75. Varnava, N. & Vanderbilt, D. Surfaces of axion insulators. *Phys. Rev. B* **98**, 245117 (2018).

Acknowledgements J.-X.Q., J.A., A.G., H.L., M.S., J.M.B., P.P.O., Q.M., R.M., R.J.M., I.M., A.V. and S.-Y.X. were supported through the Center for the Advancement of Topological Semimetals (CATS), an Energy Frontier Research Center (EFRC) funded by the US Department of Energy (DOE) Office of Science, through the Ames National Laboratory under contract DE-AC0207CH11358. The work in S.-Y.X. group was supported by CATS (task that CATS supported) and the Air Force Office of Scientific Research (AFOSR) grant FA9550-23-1-0040 (data analysis and manuscript writing). S.-Y.X. acknowledges the Sloan Foundation and Corning Fund for Faculty Development. S.-Y.X. and D.B. were supported by the National Science Foundation (NSF) career grant number DMR-2143177. Bulk single-crystal growth and characterization at UCLA were supported by the US DOE, Office of Science, Office of Basic Energy Sciences (BES) under award number DE-SC0021117. J.S.-E. was supported by the National Science Foundation under cooperative agreement 202027 and by the by Japan Science and Technology Agency (JST) as part of Adopting Sustainable Partnerships for Innovative Research Ecosystem (ASPIRE), grant number JPMJAP2318. K.W. and T.T. acknowledge support from the JSPS KAKENHI (grant numbers 21H05233 and 23H02052), the CREST (JPMJCR24A5), JST and World Premier International Research Center Initiative (WPI), MEXT, Japan. C.F. was supported by Deutsche Forschungsgemeinschaft (DFG, German Research Foundation) through SFB 1143 (project ID 24731007) and the Würzburg-Dresden Cluster of Excellence on Complexity and Topology in Quantum Matter-ct.qmat (EXC 2147, project number 390858490). H.L. acknowledges the support by Academia Sinica in Taiwan under grant number AS-iMATE-113-15. T.-R.C. was supported by National Science and Technology Council (NSTC) in Taiwan (programme number MOST111-2628-M-006-003-MY3 and NSTC113-2124-M-006-009-MY3), National Cheng Kung University (NCKU), Taiwan, and National Center for Theoretical Sciences, Taiwan. This research was supported, in part, by the Higher Education Sprout Project, Ministry of Education to the Headquarters of University Advancement at NCKU. T.-R.C. thanks the National Center for High-performance Computing (NCHC) of National Applied Research Laboratories (NARLabs) in Taiwan for providing computational and storage resources. The work at Northeastern University (A.B. and B.G.) was supported by the National Science Foundation through the Expand-QISE award NSF-OMA-2329067 and benefited from the resources of Northeastern University's Advanced Scientific Computation Center, the Discovery Cluster, the Massachusetts Technology Collaborative award MTC-22032, and the Quantum Materials and Sensing Institute. For the computational work at S.N. Bose National Center for Basic Sciences (SNBNCBS), B.G. acknowledge National Supercomputing Mission (NSM) for providing computing resources of 'PARAM RUDRA' at SNBNCBS, Saltlake, Kolkata-700106, India, which is implemented by C-DAC and supported by the Ministry of Electronics and Information Technology (MeitY) and Department of Science and Technology (DST), Government of India. J.M.B. and R.M.S experimental activities were performed at the National High Magnetic Field Laboratory, which is supported by National Science Foundation Cooperative Agreement number DMR-2128556 and the State of Florida. D.J.E.M. is supported by an Ernest Rutherford Fellowship (ST/T004037/1) and by a Science and Technologies Facilities Council grant (ST/X000753/1). Q.M. also acknowledges support from National Science Foundation (NSF) CAREER award DMR-2143426 and a Sloan Fellowship. O.L., I.P., E.M.B. and P.N. were supported by the Quantum Science Center (QSC), a National Quantum Information Science Research Center of the US Department of Energy (DOE). O.L., I.P., E.M.B. and P.N. also acknowledge support from Gordon and Betty Moore Foundation grants 8048 and 12976, and from the John Simon Guggenheim Memorial Foundation (Guggenheim Fellowship).

Author contributions S.-Y.X. conceived the experiments and supervised the project. J.-X.Q. fabricated the devices, performed the measurements and analysed data with help from A.G., C.T., H. Li, Y.-F.L., D.B., T.D., T.H., J.M.B., C.F., Q.M., R.M. and R.J.M. T.Q. and N.N. grew the bulk MnBi_2Te_4 single crystals. B.G., Y.-Y.X., M.S., J.A., I.P., O.L., E.M.B., P.N., T.-R.C., A.B., H. Lin, P.P.O., I.M. and A.V. conducted the theoretical studies including first-principles calculations and effect modelling. K.W. and T.T. grew the bulk hexagonal BN single crystals. J.S.-E., J.-X.Q., K.C.F., D.J.E.M. and S.-Y.X. made the calculation of sensitivity for dark-matter axion detection. S.-Y.X. and J.-X.Q. wrote the paper with input from all authors.

Competing interests The authors declare no competing interests.

Additional information

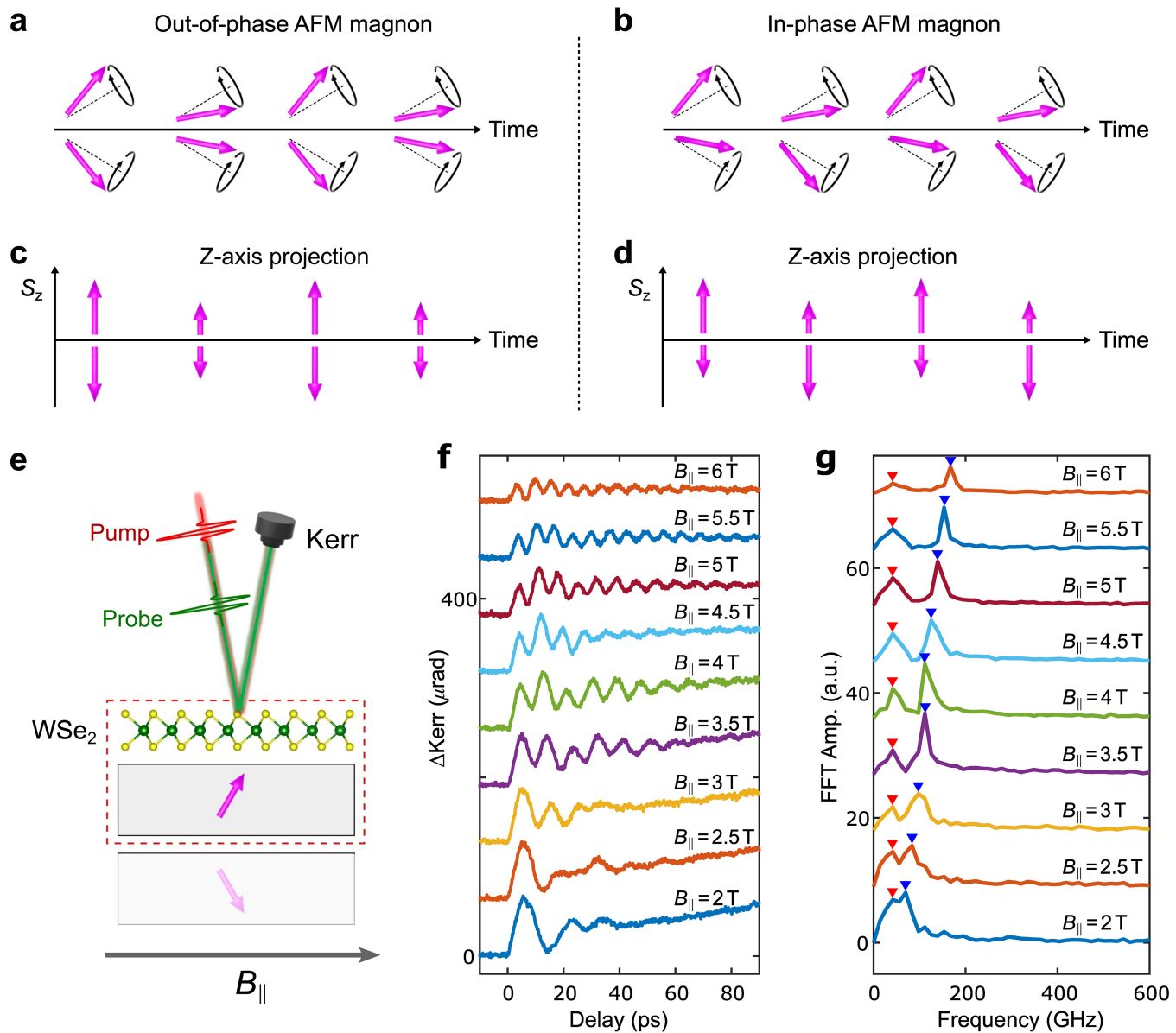
Supplementary information The online version contains supplementary material available at <https://doi.org/10.1038/s41586-025-08862-x>.

Correspondence and requests for materials should be addressed to Su-Yang Xu.

Peer review information *Nature* thanks Luyi Yang, Haijun Zhang and the other, anonymous, reviewer(s) for their contribution to the peer review of this work.

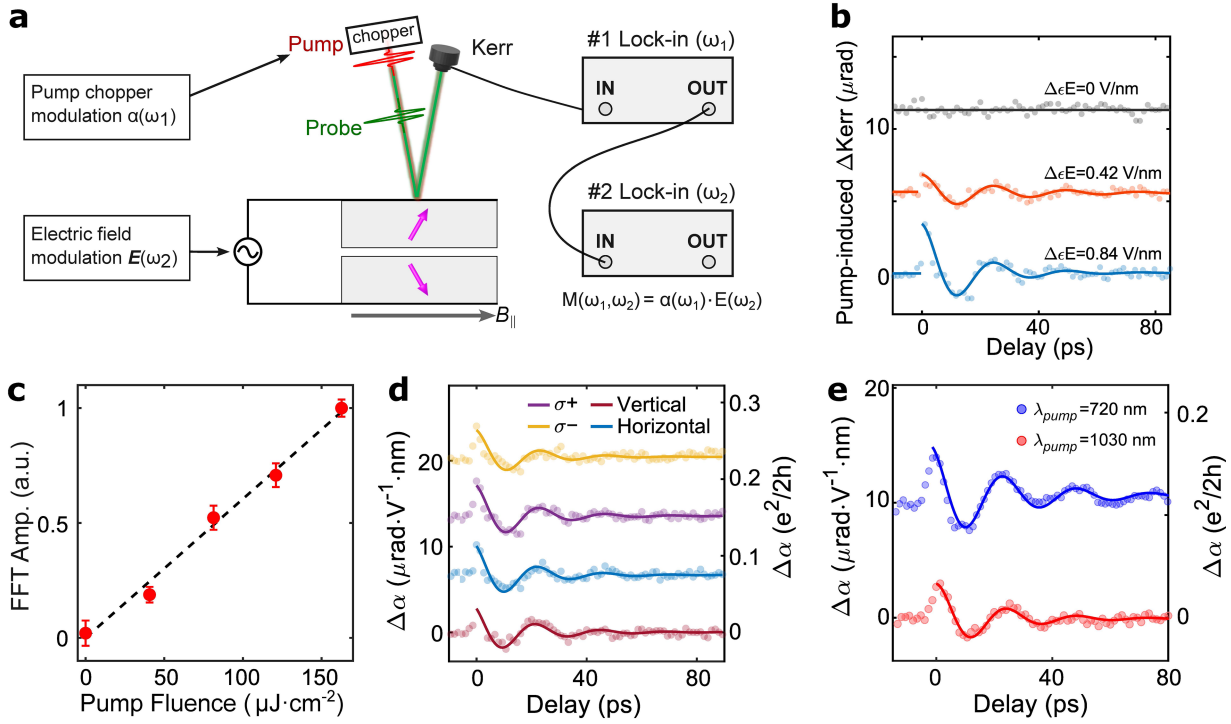
Reprints and permissions information is available at <http://www.nature.com/reprints>.

Article



Extended Data Fig. 1 | Characterization of the magnon frequency in 6-layer MnBi_2Te_4 . **a**, Time evolution of out-of-phase magnon. **c**, \hat{z} projection of the out-of-phase magnon, which resembles the antiferromagnetic amplitude mode. **b,d**, Same as panels (a,c) but for in-phase magnon, which features an oscillation of net magnetization along \hat{z} . **e**, We followed the method established in ref. 53 (see detailed discussion in Methods.2). A monolayer WSe_2 was stacked

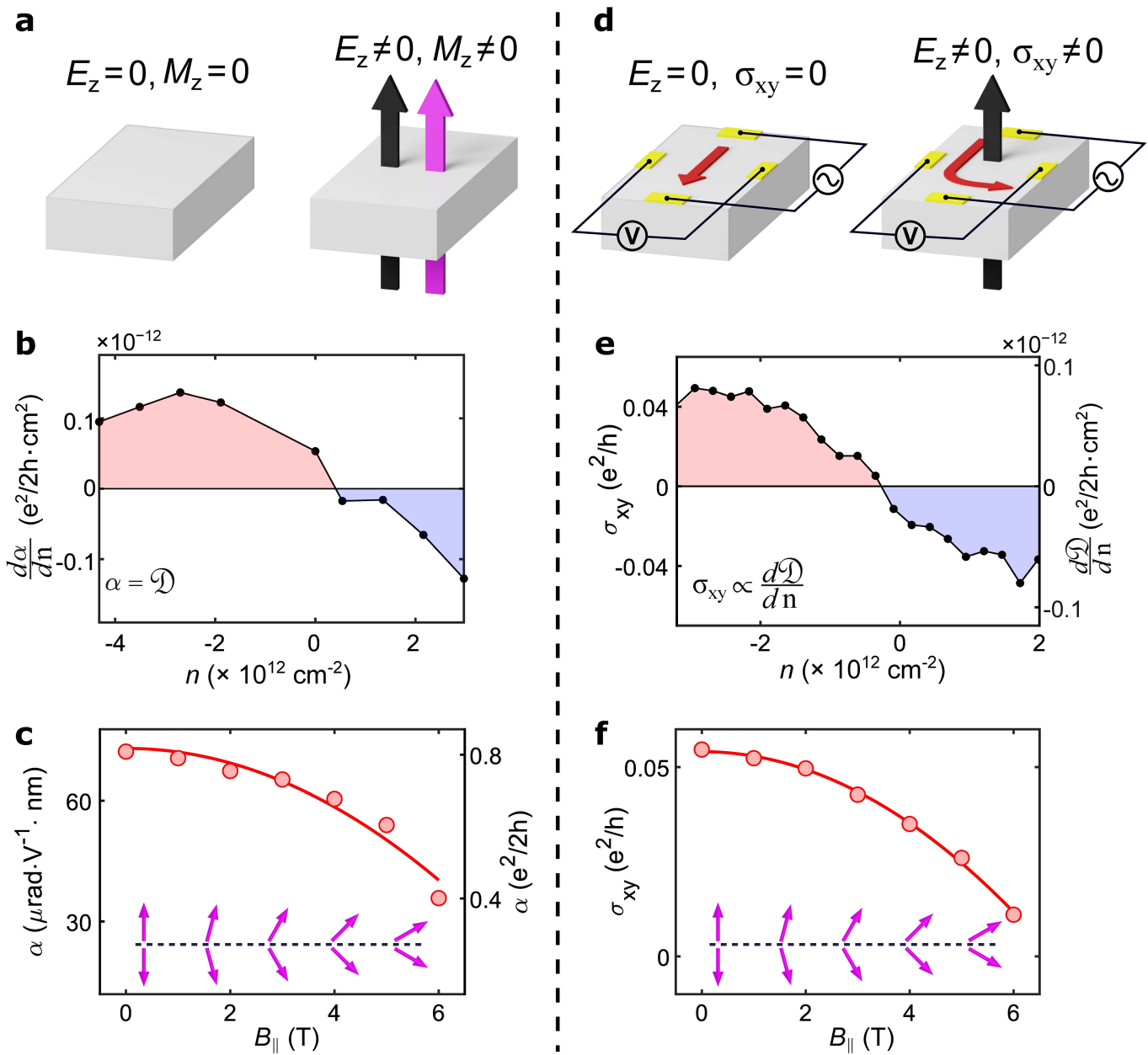
on top of MnBi_2Te_4 , which breaks the layer degeneracy, allowing us to selectively probe the top layer information⁵³. Pump-probe Kerr rotation under normal incidence was performed on this heterostructure. The pump laser launches the magnons. The probe Kerr rotation measures the out-of-plane magnetization M_z of the top layer preferentially because of the WSe_2 . **f,g**, Pump-induced ΔKerr data and FFT at different $B_{||}$.



Extended Data Fig. 2 | Experimental setup for measuring the DAQ. **a**, The DAQ manifests as a coherent oscillation of the magnetoelectric coupling, which requires us to measure $\alpha(t)$ with fs time-resolution. This was achieved by combining ultrafast pump-probe optics with 2D electronic devices. We built a dual-gated 6L MnBi₂Te₄ device (no WSe₂). The probe beam combined with the gate-applied E_z measures α , whereas the pump beam excites the magnons. By varying the delay time t , we can measure $\alpha(t)$ with fs time-resolution. Experimentally, this was achieved by connecting two lock-in amplifiers. An optical chopper modulated the pump laser at frequency $\omega_1=1000$ Hz. A functional generator modulated the gate E_z at frequency $\omega_2=0.7$ Hz.

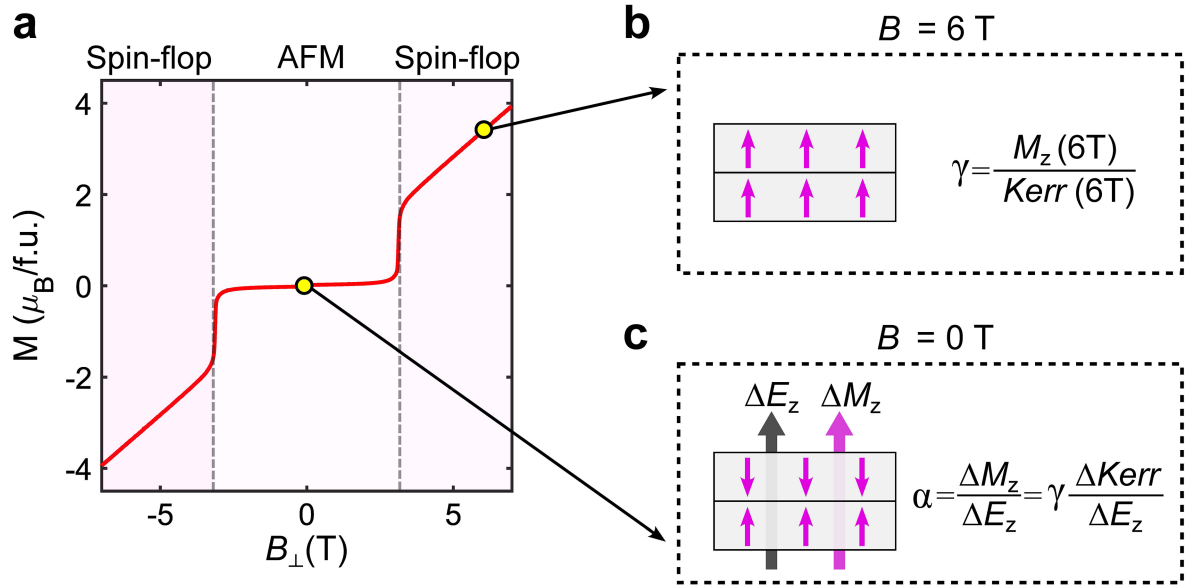
The signal collected by the balanced photodiode detector was first fed into a lock-in at the chopper frequency $\omega_1=1000$ Hz and then into the second lock-in at the E_z frequency $\omega_2=0.7$ Hz. The wavelength of the pump beam was set to 1030 nm, and the pump fluence is $\sim 160 \mu\text{J}/\text{cm}^2$. **b**, Pump-induced Kerr rotation at different AC E field modulation amplitudes. **c**, Pump fluence dependence of the oscillation amplitude of $\Delta\alpha$. **d**, Coherent oscillation of $\Delta\alpha$ as a function of pump light polarization. The indifference of pump light polarization suggests excitation mechanism is laser heating induced coherent oscillation of spins³⁰. **e**, Coherent oscillation of $\Delta\alpha$ as a function of pump wavelength.

Article



Extended Data Fig. 3 | The magnetoelectric coupling and the layer Hall effect in MnBi_2Te_4 . **a**, Schematics for the magnetoelectric coupling ($\alpha = \frac{M_z}{E_z}$). **b**, Maintext Fig. 4b shows the measured α as a function of the charge density n . By taking a derivative of this data, we get $\frac{d\alpha}{dn}$ as a function of n . **c**, Measured α as a function of in-plane magnetic field $B_{||}$. **d**, Schematics for the layer Hall effect.

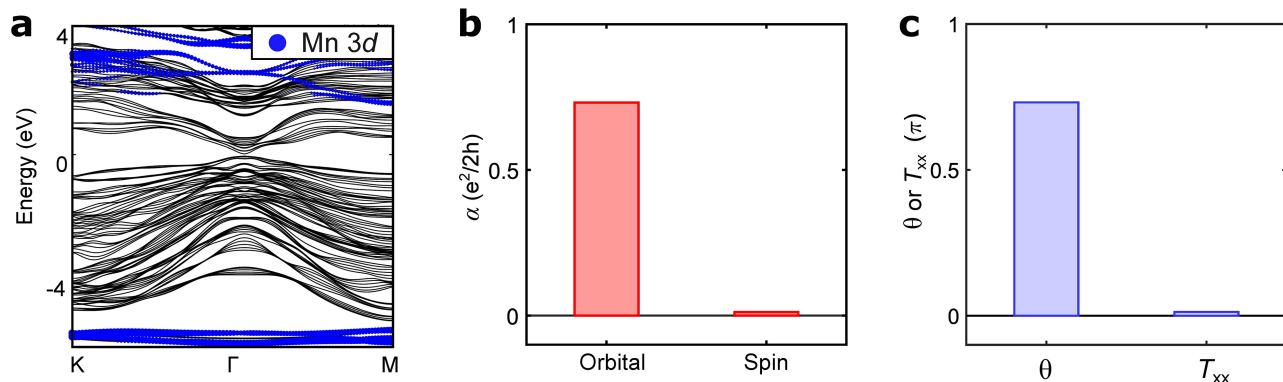
An out-of-plane electric field E_z induces an anomalous Hall effect (finite σ_{xy}) in 6L MnBi_2Te_4 . **e**, E_z induced σ_{xy} as a function of carrier density n . This E_z induced σ_{xy} directly measures $\frac{d\mathcal{D}}{dn}$ (\mathcal{D} is the Berry curvature real space dipole), which is marked in the right axis. **f**, E_z induced σ_{xy} as a function of $B_{||}$.



Extended Data Fig. 4 | Determining the conversion factor γ . **a**, Out-of-plane magnetization as function of out-of-plane magnetic field B_\perp for bulk MnBi_2Te_4 measured by SQUID. With increasing B_\perp , the magnetic order changes from the layered antiferromagnetic state to a spin-flop state. **b**, In the spin-flop state at $B_\perp = 6 \text{ T}$, we measured both the Kerr rotation and the M_z , from which we determined the value of γ . **c**, In the antiferromagnetic ground state at $B_\perp = 0 \text{ T}$,

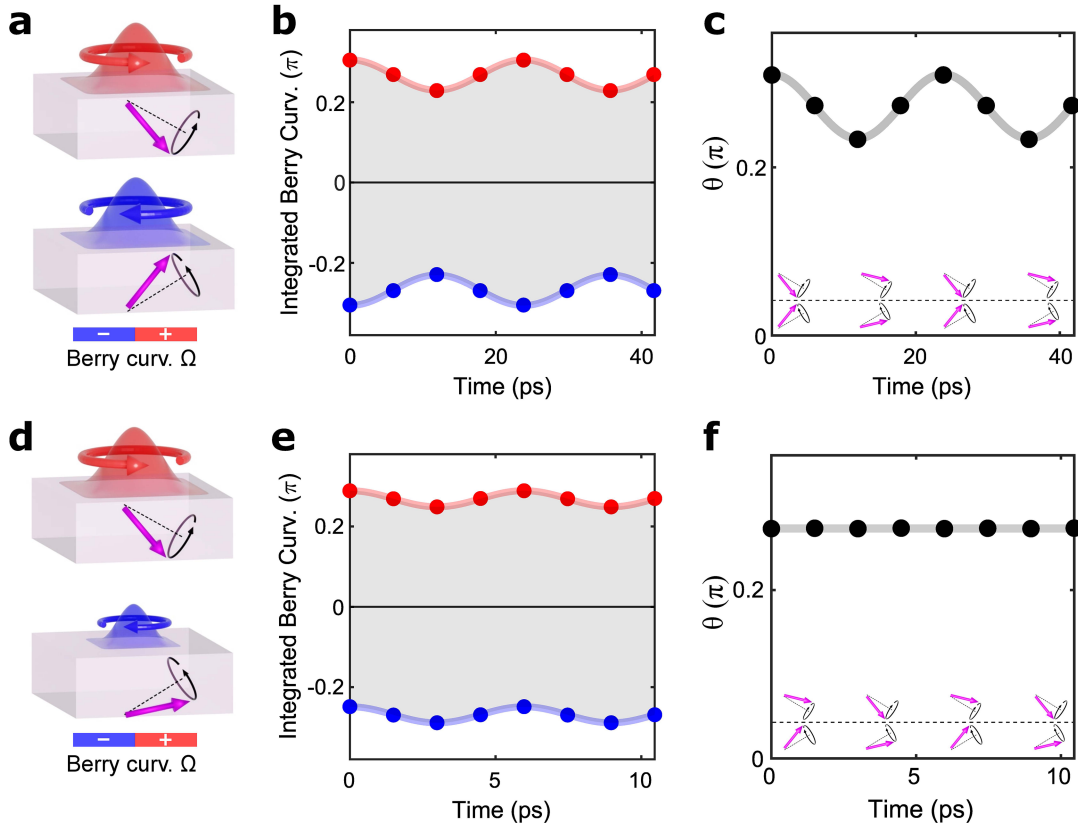
$6\text{L MnBi}_2\text{Te}_4$ features an electric field induced magnetization. The magneto-electric coupling α is given by $\alpha = \gamma \frac{d\text{Kerr}}{dE_z}$. Therefore, by using the γ determined in the spin-flop state, we converted α of the antiferromagnetic state to the unit of $\frac{e^2}{2h}$. In this method, we needed to assume that the spin flop state at $B_\perp = 6 \text{ T}$ and the antiferromagnetic state at $B_\perp = 0 \text{ T}$ have the same γ . This is an approximation.

Article



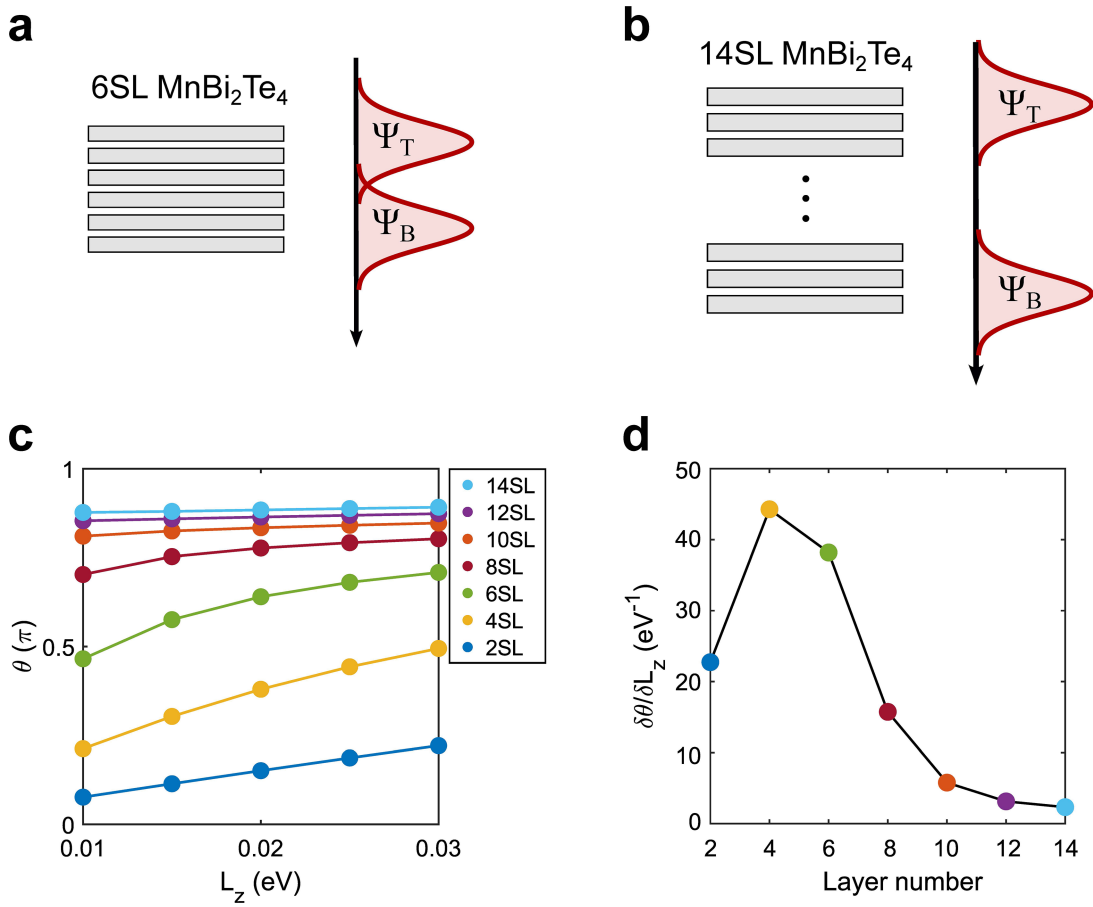
Extended Data Fig. 5 | Microscopic mechanism for the magnetoelectric coupling in 6L MnBi_2Te_4 . **a**, First-principles band structures of 6L MnBi_2Te_4 with the Mn 3d orbitals highlighted. **b**, Calculated α_{zz} from the spin and orbital

contributions. The total α_{zz} is the sum of the two contributions. **c**, Comparison of θ and T_{xx} , which are the trace part and traceless part of α_{ii} , respectively (normalized by $e^2/2h$).



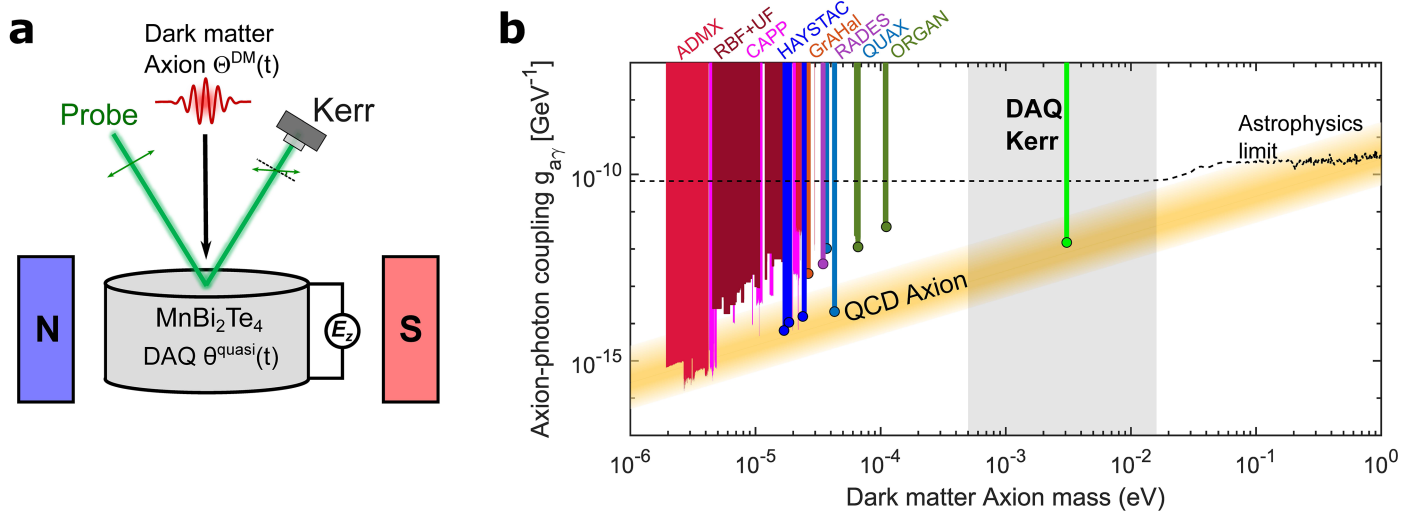
Extended Data Fig. 6 | Ultrafast Berry curvature oscillation by antiferromagnetic magnons. **a,d**, In the even-layer MnBi_2Te_4 , the antiferromagnetic order couples to the Dirac surface states, generating large Berry curvature on the top and bottom surfaces. We study how the Berry curvature responds upon exciting the out-of-phase or the in-phase magnon.

b,e, Calculated Berry curvature sum of the top and bottom surfaces at different spin angles during the magnon oscillation under the frozen magnon approximation. The grey area (i.e., the difference of Berry curvature from top and bottom surfaces) is the Berry curvature real space dipole \mathcal{D} ($\mathcal{D} = \alpha$). **c,f**, Calculated θ at different spin angles during the magnon oscillation.

**Extended Data Fig. 7 | Calculated DAQ strength of 2D even-layer MnBi_2Te_4 .**

The strength of DAQ is measured by the change of θ per change of the antiferromagnetic order parameter L_z , $\frac{\delta\theta}{\delta L_z}$. In 2D even-layer MnBi_2Te_4 , the top and bottom surface state wavefunction can overlap and hybridize. This hybridization gap competes with magnetism induced Zeeman gap,

which leads to a large but non-quantized θ . We theoretically study the $\frac{\delta\theta}{\delta L_z}$ by calculating θ as a function of L_z for different thicknesses. **a,b**, Wavefunction hybridization for 6SL and 14SL. **c**, Calculated θ vs. AFM order L_z for different thicknesses. **d**, $\delta\theta/\delta L_z$ as a function of thickness.



Extended Data Fig. 8 | Kerr effect scheme of dark matter axion detection using DAQ. **a**, The Kerr effect scheme: a dark matter axion resonantly excite an axion polariton inside the DAQ material under an external $B_{||}$ field ($B_{||}=5\text{ T}$). The axion polariton is essentially a coherent oscillation of $\theta(\omega)$, where $\omega=\sqrt{m_{\text{DAQ}}^2+b^2}$. By applying an out-of-plane electric field E_z , such a coherent oscillation of $\theta(\omega)$

will lead to an oscillating magnetization $M_z(\omega)=\theta(\omega)E_z$. We propose to use MOKE with to measure this oscillating magnetization. **b**, Dark matter detection sensitivity (g_a) as a function of the axion mass using the Kerr scheme (see details in Methods.6).